Analysis of Air Flow Distribution and Thermal Comfort in a Hybrid Electric Vehicle

by

Ningbai Ningbai

B.Eng., Zhejiang University, 2011

Thesis Submitted in Partial Fulfillment of the
Requirements for the Degree of
Master of Applied Science

in the

School of Mechatronics Systems Engineering
Faculty of Applied Sciences

© Ningbai Ningbai 2014

SIMON FRASER UNIVERSITY

Fall 2014

Approval

Name:	**Ningbai Ningbai**
Degree:	**Master of Applied Science**
Title of Thesis:	***Analysis of Air Flow Distribution and Thermal Comfort in a Hybrid Electric Vehicle***
Examining Committee:	**Chair:** Dr. Carolyn Sparrey Assistant Professor

Majid Bahrami
Senior Supervisor
Associate Professor

John Jones
Supervisor
Associate Professor

Krishna Vijayaraghavan
Internal Examiner
Assistant Professor

Date Defended/Approved: November 18, 2014

Partial Copyright License

SFU

Abstract

Energy efficiency in Hybrid Electric Vehicles (HEV) affects the vehicle mileage and battery durability. Air conditioning is the most energy consuming system after the electric motor in HEVs. Air flow distribution and thermal comfort in an HEV is studied and simulations are performed to investigate the optimum air distribution pattern for providing thermal comfort while maintaining energy efficiency.

To acquire a preliminary understanding of the problem, an analytical model is developed for air flow in a cavity. In the next step, a testbed is developed and different air conditioning scenarios are experimented. For numerical simulations, several turbulence models are verified with the experimental data and the realizable $k-\varepsilon$ model is selected. After validation, the numerical model is applied to various air conditioning scenarios inside the eVaro cabin. It is concluded that optimum air distribution patterns exist for different thermal loads and personalized ventilation can improve energy efficiency by 30% when only driver is on board.

Keywords: Hybrid Electric Vehicle; Computational Fluid Dynamics; Thermal Comfort; Air Conditioning; Energy Efficiency; Predicted Mean Vote (PMV)

I dedicate this thesis to my parents who have supported me throughout my life with their unconditional love and great patience. With faith, they set me free to chase my dream. With coddle, they open their arms to me whenever I need a break. There are many people who judge me through how far I go. But they are the people who appreciate my effort regardless of the achievement.

Acknowledgements

Table of Contents

List of Tables

x

List of Figures

List of Acronyms

CFD	Computational Fluid Dynamics
DAQ	Data Acquisition
ES	Energy Simulation
FVT	Future Vehicle Technologies
HEV	Hybrid Electric Vehicle
HVAC	Heating, Ventilation, and Air Conditioning
LAEC	Laboratory for Alternative Energy Conversion
MAC	Mobile Air Conditioning
MV	Mixing Ventilation
PEV	Plug-in Electric Vehicle
PIV	Particle Image Velocimetry
PMM	Physiological Manikin Model
PMV	Predicted Mean Vote
PV	Personalized Ventilation
SFU	Simon Fraser University
UDF	User Defined Function
VCR	Vapour Compression Refrigeration

Glossary

c	Air specific heat $kJ/(kg \cdot K)$
e	Internal energy J
F	Body force N/m^3
f_{cl}	Clothing surface factor
h_c	Convective heat transfer coefficient $W/(m^2 \cdot K)$
I_{cl}	Clothing insulation level $m^2 \cdot K/W$
k	Thermal conductivity $W/(m \cdot K)$
m	Cabin air mass kg
M	Metabolic rate W/m^2
p	Pressure Pa
p_a	Water vapour partial pressure Pa
q	Heat transfer rate W/m^2
q_c	Convective heat transfer rate W/m^2
q_r	Radiation heat transfer rate W/m^2
Q	Heat source W/m^3
$\dot{Q}$	Total heat gain W
t	Time s
T	Temperature K
t_a	Air temperature $°C$
t_{cl}	Clothing surface temperature $°C$
t_r	Mean radiant temperature $°C$
u_*	Friction velocity m/s
v_{ar}	Relative air velocity m/s
W	Effective mechanical power W

x	Horizontal coordinate cm
y	Vertical coordinate cm
y^+	Boundary criterion

Greek Letters

Φ	Heat dissipation rate W
ρ	Density kg/m^3
σ	Standard deviation
τ	Shear stress Pa
ν	Kinematic viscosity m^2/s

Subscripts

c	Variable
$\bar{c}$	Variable average value
i	Case name

Executive Summary

Air flow distribution and thermal comfort in a hybrid electric vehicle are studied and simulations are performed to investigate the optimum air distribution pattern for providing thermal comfort while maintaining energy efficiency. A systematic approach is followed and analytical, experimental, and numerical methods are used to find the most efficient air distribution pattern.

An analytical model of air flow inside a cavity is developed. Based on the results acquired from the analytical model, experimental tests are designed. A testbed is built to mimic the cabin of a vehicle. The testbed consists of a heater-fan installed inside a chamber enclosure which is attached to a ventilation unit. Temperatures at the chamber walls, inlet air, and some points inside the chamber are recorded. In addition, the heater power and fan velocity are measured. Four scenarios with different heater-fan input are tested and the results are reported.

To develop a valid numerical model, the geometry of the experimental testbed is modelled using ANSYS FLUENT software. The four experimental scenarios are simulated numerically and different grid distribution and turbulence models are examined. The numerical results are compared with the experimental data.

The chosen numerical model is used for the analysis of the vehicle cabin model. The cabin is divided into the driver seat and passenger seat regions, and asymmetrical ventilation is considered for the sake of energy efficiency. Seven steady-state scenarios are tested for studying the driver seat thermal comfort level, while fifteen simulations are performed for the passenger seat. The location of inlet and outlet, the air flow rate of inlets, and the direction of inlet air velocity are incorporated in the study scenarios. The simulation results are evaluated through their corresponding energy consumption and PMV values. In addition, a transient case study is performed to estimate the pull-down time to the steady-state temperature. An optimized air flow distribution is shown to exist that produces the best thermal comfort level as well as energy efficiency.

Chapter 1.

Introduction

1.1. Background

As vehicles become an indispensable part of everyday life, people spend 1-10 hours each day in vehicle [1]. Therefore the thermal comfort of passengers draws more and more attention. The first milestone was set when the initial Heating, Ventilation and Air Conditioning (HVAC) system for vehicles was tested on the run in 1933 in New York, US [2]. Over time, HVAC systems have become one of the most demanded features for choosing vehicles by consumers.

Vehicle fuel consumption is affected by air conditioning in large scales. Air conditioning systems can reduce the fuel economy of today's mid-sized vehicles by more than 20% while increasing NOx by approximately 80% and CO by 70% [3]. During regular commuting, the HVAC power consumption of mid-sized cars is estimated to be higher than 12% of the total vehicle power [4]. HVAC is a critical system for Hybrid Electric Vehicles (HEV), as it is the second most energy consuming system after the electric motor [5]. The energy required to provide cabin cooling for thermal comfort can reduce the range of Plug-in Electric Vehicles (PEV) from 35% to 50% depending on outside weather conditions [3].

Maintaining thermal comfort is a key in vehicle HVAC design. However, the energy consumption of the air conditioning system needs to stay within efficient boundaries. One major parameter in the design of vehicle HVAC systems is the pattern of air distribution inside the cabin. In this chapter, various aspects of the study of Mobile Air Conditioning (MAC) are discussed and the effect of air distribution on thermal comfort and HVAC energy consumption is investigated in the next chapters.

1.1.1.   Thermal Comfort

The expression "thermal comfort" came into life along with the development of HVAC systems. In 1962, six factors were defined as effective parameters of thermal comfort [6]. They are air temperature, air velocity, relative humidity, mean radiant temperature, clothing insulation, and activity level *i.e.* metabolic rate. "Thermal comfort" is defined by the American Society of Heating Refrigeration and Air Conditioning Engineers (ASHRAE) as "the state of mind that expresses satisfaction with the surrounding environment" [7]. A number of indices for evaluating the thermal comfort level are proposed according to this definition. One of the most popular and internationally accepted indices is the Predicted Mean Vote (PMV), which is applied in the analysis of the present study. Please find more information about the calculation of PMV at subsection 4.1.4.

Thermal comfort not only affects the energy consumption of the HVAC system [8], but is also a key parameter for passenger health [9], [10]. It contributes to safe driving by reducing the driver stress, avoiding windshield fogging, and guaranteeing good visibility. In addition, it is believed that achieving an improved thermal comfort system will lead to substantial cost reductions. For instance, asymmetrical thermal environments, such as Displacement Ventilation (DV) or Personalized Ventilation (PV), have been developed in recent years [11], [12]. Compared to Mixing Ventilation (MV), PV can reduce the cooling power supply by approximately 75% and heating power demand by approximately 61% in building HVAC system [13].

1.1.2.   Thermal Loads in Vehicle Cabins

Calculation of the heating/cooling loads is a prerequisite for designing a proper air conditioning system. The thermal loads are imposed to the vehicle cabin through various mechanisms. Generally, the thermal loads in the cabin are calculated based on a heat balance of the incoming thermal energy from different sources.

Fayazbakhsh and Bahrami [14] categorized the thermal loads into several mechanisms, namely metabolic, radiation, ambient, ventilation, air conditioning, engine, and exhaust load. Zheng *et al.* [15] devised a simple method to calculate vehicle's thermal loads. They calculated the different loads such as the radiation and ambient

loads. A case study was performed and the results were validated using wind tunnel climate control tests. The different loads were separately calculated and summed up to give the total heat gain or loss from the cabin. Arici *et al.* [16] developed a computer code for simulating the dynamic operation of a climate control system for a typical vehicle. They considered the transition of both the cabin temperature and the relative humidity as predicted by the principles of heat and mass transfer; a lumped system model was developed. Selow *et al.* [17] developed a virtual vehicle based on experimental correlations for each significant vehicle component. The virtual vehicle was divided into different modules, one of which was the cabin climate. Such simultaneous operation of these modules could provide estimations without necessitating cumbersome and costly experiments. Khayyam *et al.* [18] collected a set of models to calculate the different types of thermal loads encountered in a vehicle. These models were later used to estimate the overall cooling load which was fed to a coordinated energy management system to reduce the air conditioning energy consumption. Wei and Dage [19] developed an intelligent cabin climate control system based on human-sensory response to comfort factors. They used passive remote infrared sensors to measure passenger skin temperatures. An intelligent climate controller then controlled the parameters such as the blower speed to provide passenger thermal comfort.

A common method for calculation of the thermal loads consists of an Energy Simulation (ES) of the cabin. In this method, a bulk zero-dimensional model of the vehicle cabin is considered. The entire cabin is assumed to have one representative temperature and relative humidity. Thus, no information on the spatial distribution of velocity and temperature is available and/or achieved in ES methods. Numerical simulation of the air distribution in the cabin can provide more detailed analysis of the velocity and temperature field which, in turn, improves the calculation of thermal loads in the vehicle cabin. In this study, CFD simulations of air flow and heat transfer inside the vehicle cabin are studied and 3D detail results are reported.

1.1.3.   *Energy Consumption of Mobile HVAC Systems*

In a vehicle HVAC system, the heating process mostly uses the waste heat from engine, while the cooling process in most light-duty vehicles relies on shaft power by

80% and the remaining 20% is the electricity provided by an alternator. The typical peak cooling load required for pulling down the temperature of a sedan is around 6 kW in a hot soak scenario, which is comparable to that of a residential house [20]. According to the estimation of US Environmental Protection Agency [21], an oversized HVAC system consumes 2.6 to 4.1% of the automotive fuel consumption, and the cost of heating and cooling in a car can be as expensive as in a house [22].

However, a favorable thermal comfort level in a car cabin is not necessarily achieved by excessive energy consumption and high expenses. An efficient air flow distribution system can provide a comfortable driving environment with a decreased size of HVAC system.

1.1.4. eVaro Car Model

The vehicle model studied in this work is a 3-wheeled 2-seated hybrid electric vehicle designed by Future Vehicle Technologies (FVT) [23]. The vehicle name is eVaro (Figure 1.1). The hybrid vehicle has a specific design and shape for advantages in hydrodynamics and stability. It is designed for speed, low noise, sustainability, and efficiency. A 200 km trip in eVaro can be entirely powered by electricity, and additional gas generator can be used for mileage increase. Thus, 90% of regular daily commutes can be travelled with zero emission.

Figure 1.1.   eVaro car model

eVaro does not have an HVAC system installed on it. It is the goal of this study to assist the design of its HVAC system through analysis of the proper inlet and outlet duct sizes and locations. Due to the specific geometry and the unique design of eVaro, implementation of conventional air flow distribution systems that are normally performed for 4-seat passenger vehicles is not practical for eVaro. Hence, a study on the air distribution in the mentioned tandem seat arrangement is performed in this work.

1.2. Numerical Studies on Air Flow Distribution

Air flow distribution studies cover a wide range of applications such as jet flow behavior, contamination spread, and cooling and heating processes. In the last century, theoretical and analytical studies on air flow distribution have reached a mature level. Common phenomena such as jet flow and plume are solved analytically with highly accurate solutions [24]. However, as emerging technologies brought more complicated problems to be solved, analytical approaches seemed insufficient, particularly when a relatively complex geometry is involved. Hence, researchers looked for an alternative way and Computational Fluid Dynamics (CFD) shed a light on it in accordance with the growth of computational capacity.

Numerical simulation is generally less expensive and less time-consuming than experimental approaches. However, the reliability of numerical methods relies on many factors, such as grid distribution and model selection. Hence, researchers tend to combine experimental approaches with numerical methods when they investigate complicated problems with multi-physics processes [25].

The process of the air flow distribution study in this work can be summarized as follows:

- Conducting a few specific cases of experiments.

- Selecting key parameters for numerical simulation, such as mesh size, turbulence model and etc.

- Running numerical models with different combinations of key parameters for specific cases.

- Validating numerical models with experimental data.

- Using the selected numerical model for further study.

In the following sections, the basics of CFD and the previous numerical works on air flow distribution in vehicle cabins are introduced.

1.2.1. Turbulence Model Selection

The air flow in a vehicle cabin is mostly turbulent. For numerical simulation of air flow distribution in cavities with complicated geometries, selection of the turbulence model is a key factor for proper numerical simulations. Different turbulence models are used in previous air flow distribution studies [26]–[31]. They differ from each other with respect to grid-dependency, time consumption, and accuracy, to name a few. From the engineering point of view, it is well known that different applications have different focuses and requirements. In order to get an acceptable simulation result with the least resources, researchers have compared different turbulence models for more specific purposes of air flow distribution study, as shown in Table 1.1. Table 1.1 also shows the model recommended by each of the studies. Some researchers [32]–[34] have aimed at refrigerated trucks, while others [35]–[37] have studied air distribution in residential rooms.

In addition, the near-wall treatment of mesh for turbulence models is one of the most significant parameters that influence the accuracy of airflow simulation. A criteria called y^+ is introduced to measure the effect of the distance of the first node from the wall surface. Studies [38], [39] have shown that choosing the right combination of the wall treatment method and turbulence can significantly improve the accuracy of the numerical simulation.

Table 1.1.   Summary of a number of studies on turbulence model selection

Turbulence Model	Reference			
	[32], [33], [35]	[34]	[36]	[37]
Standard $k - \varepsilon$	√	√	√	√
RNG $k - \varepsilon$		√	√	√

6

Turbulence Model	Reference			
	[32], [33], [35]	[34]	[36]	[37]
Realizable $k - \varepsilon$			√	
Standard $k - \omega$			√	
SST $k - \omega$			√	
RSM	√	√		
Model recommended	RSM	RSM	RNG $k - \varepsilon$	RNG $k - \varepsilon$

1.2.2.   Numerical Study

The study of air-flow distribution is a mature subject and the literature related to this subject is numerous. Previous studies have shed light upon the problems, such as aircraft cabins, car cabins, buildings, and so on (Table 1.2), aiming at the investigation of thermal comfort and contaminant spreading.

Table 1.2.   Summary of literature on air flow distribution and thermal comfort

Application	Study	Method	Notes and Highlights
Aircraft	Yan *et al.* [26]	Experimental and numerical	Turbulence model: Standard $k - \varepsilon$
	Zhang and Chen [27]	Experimental and numerical	Turbulence model: RNG $k - \varepsilon$
	Bianco *et al.* [28]	Numerical	Turbulence model: RNG $k - \varepsilon$
	Bosbach *et al.* [30], Günther *et al.* [29]	Experimental and numerical	Experimental method: Particle Image Velocimetry (PIV); Numerical model: RANS (StarCD)
	Zhang *et al.* [31]	Experimental and numerical	Numerical model: RANS model
	Wu and Ahmed [40]	Experimental and numerical	Air supply mode studied
	Liu *et al.* [41]	Review	Review on thermal comfort studies
Vehicle	Zhang *et al.* [42], Zhang *et al.* [43]	Experimental and numerical	Thermal comfort; the relationship between the cooling load and inlet temperature, volume flow rate, etc.
	Han *et al.* [44]	Experimental and numerical	Combination of solar load, refrigeration cycle analysis, CFD and human physiology model

Application	Study	Method	Notes and Highlights
	Alexandrov [45]	Numerical	Temperature and velocity at inlets, size and location of the system's inlets and outlets, etc. studied
	Bayraktar [46], [47]	Numerical	Air distribution in military vehicles studied
	Alahmer *et al.* [48]	Review	Thermal comfort models reviewed
Building	Tong *et al.* [36]	Experimental and numerical	Five turbulence models compared
	Posner *et al.* [37]	Experimental and numerical	Turbulence model evaluation
	Yongson *et al.* [35]	Numerical	Effect of air-conditioner location studied
	Cheng *et al.* [49]	Review and numerical	Thermal comfort reviewed
	Chen [50], Chen *et al.* [51]	Review	Assessment of analytical, empirical and numerical models

Similar to vehicle applications, airplane cabin is in an isolated and extreme environment for most of its duration of operation. Therefore, air conditioning is mandatory for adjusting the airplane cabin conditions at a thermally comfortable level. Hence, aircraft cabin study is one of the hottest topics among air flow simulation studies. Experimental methods, like Particle Image Velocimetry (PIV), have been used for experimental setups to validate numerical models.

Yan *et al.* [26] applied the standard $k-\varepsilon$ turbulent model for simulation of air flow in airplane cabins. On the other hand, Zhang and Chen [27] and Bianco *et al.* [28] showed that the RNG $k-\varepsilon$ turbulent model is also an acceptable tool for simulating the cabin air flow. Liu *et al.* [41] performed a comprehensive study on state-of-the-art methods for studying air distributions in commercial airliner cabins. Numerical simulations have proved to be a cost-effective and efficient approach for HVAC design in airplane cabins.

The design of HVAC systems for buildings is a more mature engineering task compared to mobile applications. Important applications of building HVAC design include public environments, contaminant spreading in hospitals, CO_2 accumulation in theaters, accumulation of combustible gas in mines, and so on. Specifically, Yongson *et al.* [35] studied the air flow in an air conditioned room. Many instances of numerical

simulations deemed for improving air flow pattern in residential applications exist. Chen [50] reviewed many of these studies that aim at predicting the ventilation performance in residential applications.

Vehicle HVAC applications are similar to both aircraft and building applications. The same analysis approach applies to them, while vehicle applications have medium mobility and medium occupancy compared to airplane and building applications, respectively. Its features require an efficacious, quick-response, noise-free, compact and low energy-consuming HVAC system. The challenge in vehicle HVAC is to control the thermal comfort while addressing the above features.

Zhang *et al.* [42] and Zhang *et al.* [43] performed a thorough experimental and numerical study on the thermal comfort of sedan car models. The relationship between the cooling load and inlet temperature, outside temperature, air flow velocity, as well as the effect of glazing material are investigated. Han *et al.* [44] combined the solar load, refrigeration cycle analysis, CFD, and human physiology model. A simple PMV analysis was done, but it was not regarded as the main criterion for thermal comfort. In a study by Alexandrov [45], factors such as the temperature and velocity at inlets, the size and location of inlets and outlets, outdoor temperature, and air velocity were investigated. A comparison of different scenarios in terms of both the thermal comfort and energy consumption was not performed in that study. Bayraktar [46], [47] investigated the thermal management in a military vehicle compartment.

In this work, several scenarios of air distribution design for the eVaro cabin are studied. Different sizes and locations of inlet and outlet registers are considered and the various flow patterns are discussed. Numerical simulations are used as the analysis tool for the project. Both the thermal comfort and energy consumption are evaluated simultaneously to compare the scenarios. Analysis of a large number of designs in this work allows the design of the best and most efficient air distribution pattern while optimizing the HVAC energy consumption.

1.3. Objectives

The literature review indicates that the current available research is not fully considering the thermal comfort criteria. An analysis of the trade-off between thermal comfort and HVAC energy consumption is required for a sustainable approach towards designing mobile air conditioning systems. PMV is a straight-forward indication for thermal comfort. It not only considers temperature, but also involves other parameters, such as air velocity, humidity, etc. In previous studies the researchers only considered the thermal comfort with full occupancy in the vehicle cabin. However, in most occasions, there are fewer passengers on board. Therefore, personalized ventilation should be investigated in-depth, since it will definitely reduce the energy consumption of the HVAC system.

It is reported that 85% of vehicular trips involve an average distance fewer than 18 km and with durations from 15 to 30 min [52]. Hence, an efficient air flow distribution system of vehicle cabin should have a short response time as well as provide a good thermal comfort level to the driver and the passenger(s). To investigate such a flexible, energy saving and comfortable air flow distribution system, the present study performs experimental and numerical analysis on the newly developed hybrid-electric vehicle model, eVaro.

In Chapter 2, a small-scale prototype of a vehicle cabin is used for experiments. The testbed is tested for four scenarios, mainly for the temperature distribution, for the purpose of supporting the numerical model development. In Chapter 3, the testbed geometry is built and the experiments are duplicated in ANSYS FLUENT software. Important factors such as grid distribution and turbulence model selection are investigated. The numerical model is selected and validated with the help of experimental data from Chapter 2.

In Chapter 4, the geometry of eVaro is examined. A worst case scenario based on the literatures [18], [53]–[55] is considered and a series of simulations is performed to investigate different combinations of inlets and outlets locations and air flow rate. Aiming at optimizing the air flow distribution system, a systematic analysis is conducted for the

PMV distribution and energy consumption. Finally, the conclusions and suggested future works are brought in Chapter 5.

Chapter 2.

Experimental Study

The objective of the experimental study is to provide a reference for the evaluation of numerical model. To conduct this experimental investigation, an available testbed at SFU is used. Four sets of tests with different parameters are undertaken to collect the data and validate the numerical data obtained from the simulations in the next chapter.

2.1. Testbed Design

2.1.1. Experimental Setup

An available chamber is used as the testbed to perform the experiments. The components of test system include a chamber enclosure and a heater-fan. There are one inlet and one outlet on the chamber for the purpose of air ventilation. A SolidWorks schematic of the testbed is shown in Figure 2.1. The actual experimental setup is shown in Figure 2.2.

The chamber is supported by a wooden structure. It contains a glass wall at the front, a small cubic box made of acrylic at the rear where the heater-fan is placed, and the main enclosure which is curtained with Polyvinyl Chloride (PVC). The thicknesses of the glass, acrylic sheet, and PVC curtain are 3 mm, 3 mm and 0.4 mm, respectively.

The heater-fan blows the air horizontally with an automatic thermostat for temperature control. There are two power settings on the heater-fan; 750 W and 1500 W. The heater-fan, with the wooden block at the bottom for height adjustment, is placed at the middle of the acrylic box as shown in Figure 2.1.

The inlet and outlet of the PVC chamber are ventilated to an auxiliary cooling system, not shown in the schematic. For the cooling system, only the air flow rate (volumetric) and the inlet temperature are measured.

The details of the components dimensions and the locations are given in Table 2.1. The position of the origin is as shown in the schematic.

In the following chapter, a numerical model is built and the simulation results of the present testbed are validated with the experimental data. Then, the validated numerical model is implemented for the analysis of air flow distribution and thermal comfort in eVaro vehicle model.
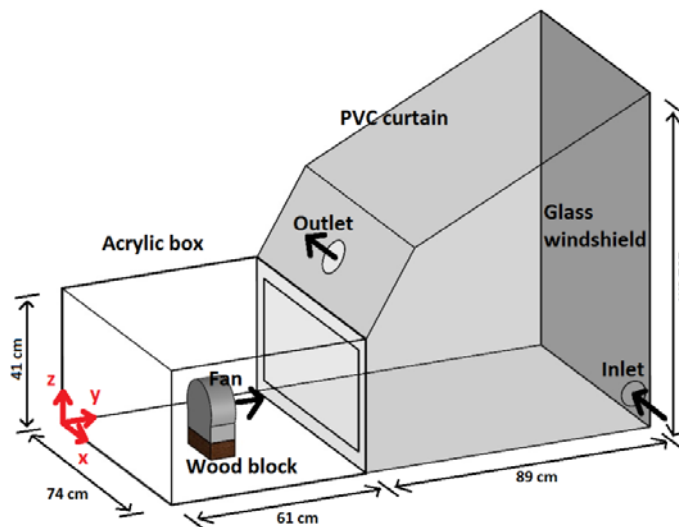
Figure 2.1.   The SolidWorks schematic of the experimental testbed

Figure 2.2.   The arrangement of experimental testbed

Table 2.1.   Locations and dimensions of components

Components	Location	Dimension
	cm	cm
Fan	(37, 30, 24)	Ø17 × 8
Wood block	(37, 30, 24)	15 × 8 × 5
Inlet	(74, 146, 11)	Ø 8
Outlet	(37, 67, 54)	Ø 10

2.1.2.   Measurement Components

Heater Power and Fan Velocity Measurement

In the experiments, the heater-fan is set to lower power level (750 W), while it is plugged to a convertible power supply (SC-20MVariac). The actual voltage and current of the supplied power are measured with two multimeters (Extech 430, as shown in Figure 2.3).

Figure 2.3.   Power supply measurement: SC-20MVariac (middle) and Extech 430 multimeters (two sides)

The fan velocities for different input powers are measured by Air Velocity Meter (VelociCalc Model 5725), shown in Figure 2.4. The average velocity value is calculated from measurements in 5 random points on the fan surface, as shown in Figure 2.5.

14

Figure 2.4.   **Anemometer**

Figure 2.5.   **Five random velocity measurement points on the fan surface**

Temperature Measurement

To measure the wall temperatures, ten thermocouples are attached to the center of the testbed walls. In addition, six Temp Track-it B Loggers from Monach Instruments are hung inside the testbed to obtain air temperature, which have an accuracy of ±1.0°C. The locations of these 6 thermocouples are shown in Figure 2.6, and the location details can be found in Table 2.2.
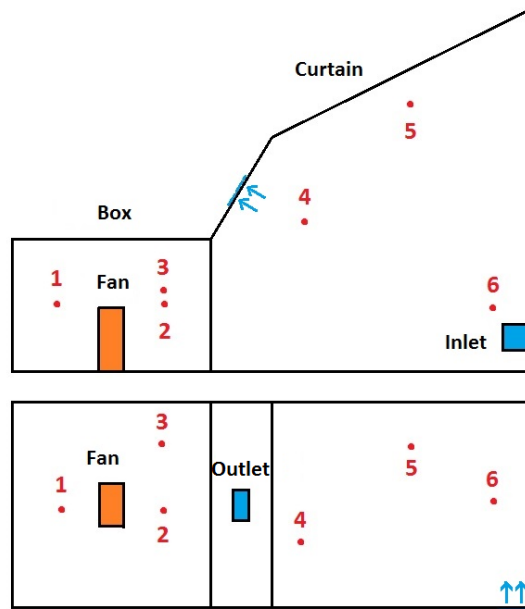
Figure 2.6. **Locations of data loggers: side view (top) and top view (bottom)**

The signal of thermocouples are monitored and recorded by computer with LabVIEW software through NI 9214DAQ system (Figure 2.7).
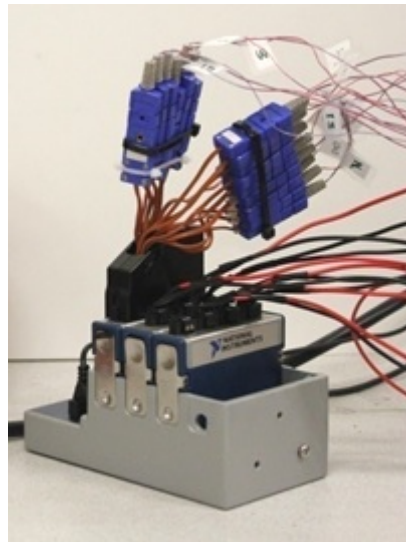
Figure 2.7. **NI 9214DAQ system**

Table 2.2. **Locations of data loggers**

Components	Location
	cm
Data logger 1	33, 14, 19
Data logger 2	11, 46, 24
Data logger 3	33, 47, 20
Data logger 4	47, 69, 29
Data logger 5	7, 90, 51
Data logger 6	18, 130, 23

2.2. Data Collection

The chamber is tested at a room temperature of $21°C$. During the experiments, the input power supplied to the heater, fan velocity, inlet air temperature, outlet air velocity, chamber wall temperature and the temperature of specified points are measured. Electrical power is applied using the AC power supply. The voltage and the current are respectively measured with Extech 430 multimeter and METRA HIT ONE PLUS multimeter to determine the power input to the heater-fan, where the fan power is negligible. The accuracy of both multimeters for voltage and current readings is 0.3%. Ten self-adhesive, T-type, copper-constantan thermocouples with the accuracy of $±1°C$ are installed at the centre of each wall. All the thermocouples are plugged into the DAQ system. Their readings are recorded on a PC through LabVIEW program till they fall within a bandwidth of 0.1°C of the steady state value. The anemometer has an accuracy of 1% $±0.2 \text{ m/s}$.

The input power of the heater-fan ranges from 391-746 W. In accordance, the velocity of fan varies from 0.98-1.80 m/s, as shown in Table 2.3. Test 2 is done without air ventilation. The inlet velocity is calculated based on the mass conservation law. It should be noted that the direction of inlet velocity is as shown in Table 2.4, where the positive sign is in accordance with the direction of the coordinates indicated in Figure 2.1. A summary of the tests is given in Table 2.5.

Table 2.3.   Heater-fan input power and fan exit velocity

Tests	Input power	Fan velocity
	W	m/s
Test 1	529.2	1.25
Test 2	600.0	1.45
Test 3	746.4	1.80
Test 4	390.7	0.98

Table 2.4.   Velocities at inlet and outlet of the chamber

Vents	Direction	Fan velocity
	cm	m/s
Inlet	-29, -9, +20	6.61
Outlet	Normal to the surface	3.73

Table 2.5.   A summary of experimental data

Component	Temperature			
	°C			
	Test 1	Test 2	Test 3	Test 4
Inlet	6	--	15	11
Box rear	24	38	29	26
Box left	25	40	31	26
Box right	24	42	30	26
Box top	25	41	30	26
Box bottom	24	37	28	24
Curtain front	16	46	20	15
Curtain left	22	41	29	21
Curtain right	22	43	27	22
Curtain top	21	38	26	20
Curtain bottom	23	46	30	21
Data logger 1	26.5	49.8	32.8	26.8

Component	Temperature °C			
	Test 1	Test 2	Test 3	Test 4
Data logger 2	25.8	52	32.8	25.8
Data logger 3	40.5	65.0	44.0	41.0
Data logger 4	25.0	53.3	33.8	25.5
Data logger 5	24.0	53.6	31.1	21.9
Data logger 6	--	--	31.5	21.3

2.3. Uncertainty Analysis

2.3.1. Outlet Velocity Measurement

As mentioned in the previous subsection, the inlet velocity is calculated from outlet velocity based on the mass conservation law. Table 2.6 shows the measurement and average value of outlet velocity measurement. The standard deviation, which is random error, is calculated with Eq. (2.1), which results in $0.1\,\mathrm{m/s}$. Since the anemometer has an accuracy of 1% $\pm 0.2\,\mathrm{m/s}$, the random error is 3.7 ± 0.3.

Table 2.6.   Outlet velocity measurement

Outlet velocity m/s							
1	2	3	4	Average	Systematic error	Random error	Final reading
3.8	3.8	3.6	3.7	3.7	0.2	0.1	3.7 ± 0.3

$$\sigma_c = \sqrt{\frac{1}{N-1}\sum (c_i - \overline{c})^2} \tag{2.1}$$

where σ is standard deviation, c is the variable, i is the name of the case, $\overline{c}$ is the average value of variable, and N is population range.

2.3.2. Fan Velocity Measurement

The same analysis applies for fan velocity. Table 2.7 shows the details from measurement.

Table 2.7.   Fan velocity measurement

Tests	Velocity								
	m/s								
	1	2	3	4	5	Average	Systematic error	Random error	Final reading
Test 1	1.1	1.4	1.3	1.4	1.1	1.3	0.2	0.2	1.3 ± 0.4
Test 2	1.4	1.5	1.5	1.7	1.2	1.5	0.2	0.2	1.5 ± 0.4
Test 3	1.6	1.8	1.9	2.0	1.6	1.8	0.2	0.2	1.8 ± 0.4
Test 4	0.9	1.1	1.0	1.1	0.8	1.0	0.2	0.1	1.0 ± 0.3

2.3.3. Fan Power Measurement

The accuracy of both multimeters for voltage and current readings is 0.3%. The systematic error of power is calculated from Eq. (2.2). The measurement details are shown in Table 2.8.

$$\frac{\delta q}{|q|} = \sqrt{\left(\frac{\delta U}{U}\right)^2 + \left(\frac{\delta I}{I}\right)^2}$$

(2.2)

Table 2.8.   Fan power measurement

Tests	Voltage	Current	Power	Systematic error	Final reading
	V	A	W	W	W
Test 1	94.0	5.63	529.2	0.4%	529.2 ± 2.1
Test 2	100.0	6.00	600.0	0.4%	600.0 ± 2.4
Test 3	111.4	6.70	746.4	0.4%	746.4 ± 3.0
Test 4	79.9	4.89	390.7	0.4%	390.7 ± 1.6

Chapter 3.

Numerical Model Development and Validation

In order to obtain reliable results from numerical simulations, many elements have to be taken into consideration. A thorough understanding of the key parameters is the basis of reliable modeling. As such, for the sake of selecting and validating the numerical model, a comprehensive numerical study of the experimental testbed is performed, to investigate the influences of mesh quality, turbulence model and etc. In the following subsections, the basics of Computational Fluid Dynamic (CFD) are briefly discussed. Then, the details of the assumptions, mesh distribution and the numerical setups are presented. At the end, the simulation results are compared against the experimental results as reported in the previous chapter, to evaluate the performance of different mesh and turbulence models.

3.1. Introduction to Computational Fluid Dynamics

Computational Fluid Dynamics (CFD) is a procedure that numerically approximates and analyses the motion of fluid. There are three key components in this procedure, which are the governing equations, computational grid (mesh), boundary conditions and initial conditions. Governing equations are the partial differential equations which describe the fluid flow. They are discretized into numerical analogue of the equations. Mesh is established when the geometry or domain is divided into small grids or elements. With the addition of boundary conditions, the discretized governing equations can be solved, mostly through iterations. In addition, there are certain control parameters involved in order to improve the convergence, stability and accuracy of the calculation.

3.1.1. Governing Equations

The motion of fluid can be described with the principles of mass, momentum and energy balance equations.

Continuity:

$$\frac{\partial \rho}{\partial t} + \nabla \cdot \left(\rho V \right) = 0 \tag{3.1}$$

Momentum:

$$\rho \frac{D\vec{V}}{Dt} = \nabla \cdot \vec{\tau}_{ij} - \nabla p + \rho \vec{F} \tag{3.2}$$

Energy:

$$\rho \frac{De}{Dt} + p \left(\nabla \cdot V \right) = \frac{\partial Q}{\partial t} - \nabla \cdot q + \Phi \tag{3.3}$$

where ρ is the fluid density, V is the fluid velocity vector, τ_{ij} is the viscous stress tensor, p is pressure, F is the body forces, e is the internal energy, Q is the heat source term, t is time, Φ is the dissipation term, and $\nabla \cdot q$ is the heat flux by conduction, which is related to temperature via Fourier's law:

$$q = -k\nabla T \tag{3.4}$$

where k is the coefficient of thermal conductivity, and T is the temperature.

3.1.2. Boundary Conditions

The boundary conditions and the initial conditions also help define a problem. In general, there are three types of boundary conditions. Dirichlet boundary condition sets known constant on the boundary. Neuman boundary condition sets known derivative on the boundary. Mixed boundary condition sets the combination of the above two types on

22

the boundary. In the present study, the first and second types of boundary conditions are used.

3.1.3. Transfer Equations

In order to solve the partial differential equations, they have to be analogized into the form that computer can program and calculate, which is called discretization. The most popular numerical discretization techniques are the finite difference method, the finite element method and the finite volume method. The present work utilizes ANSYS FLUENT software, which is one representative of the Finite Volume Method.

An example is shown in Figure 3.1 to indicate the way transfer equations work. There are three cells W, P and E, between which the interfaces are w and e. The derivatives can be written as follows:

$$\left[\frac{\partial^2 u}{\partial x^2}\right]_P = \frac{\left[\left(\frac{\partial u}{\partial x}\right)_e - \left(\frac{\partial u}{\partial x}\right)_w\right]}{x_e - x_w} \tag{3.5}$$

$$\left[\frac{\partial u}{\partial x}\right]_e = \frac{u_E - u_P}{x_E - x_P} \tag{3.6}$$

$$\left[\frac{\partial u}{\partial x}\right]_w = \frac{u_P - u_W}{x_P - x_W} \tag{3.7}$$
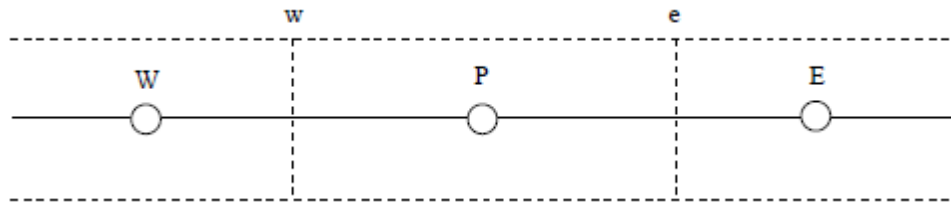
Figure 3.1.   Three cells of the Finite Volume Method

3.1.4. Mesh Generation

Types

Mesh generation is to divide the computational domain into elements. All the parameters, such as velocity, pressure, temperature, will be calculated for each element. Figure 3.2 shows the common-used element shapes for 3D simulation.

The mesh built from elements can be categorized into structured and unstructured mesh. Structured mesh transforms a body fitted non-uniform non-orthogonal physical space into an orthogonal one. A block division step is needed before determining the element divisions inside each block, and mesh parameters are fully controlled. Whereas, unstructured mesh generation is a random procedure that rigorous pre-set cannot be applied as structured mesh, and it highly conforms any geometry, but requires bigger memory to store and is prone to numerical approximation errors.

Structured mesh and unstructured mesh are implemented to the studies of present chapter and the following chapter, respectively.

4-noded tetrahedral   6-noded prism   8-noded hexahedral
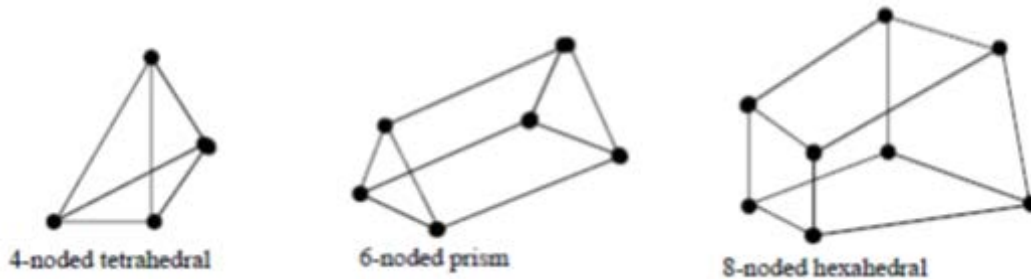
Figure 3.2.   Example of element shapes

Boundary Layer

y^+ is a parameter defined at the first layer of mesh near the wall:

$$y^+ \equiv \frac{u_* y}{\nu} \qquad\qquad (3.8)$$

where y is the distance from the wall, v is the kinematic viscosity, and u_* is friction velocity defined as:

$$u_* \equiv \sqrt{\frac{\tau_w}{\rho}} \tag{3.9}$$

with τ_w as wall shear stress and ρ as the flow density.

The flow is divided into three different regions according to y plus value, as indicated in Table 3.1. The wall shear is dominated by viscous stress in viscous sublayer, by turbulent shear in log-law region and by both viscous and turbulent shear in buffer region, respectively. Generally, the simulation gives the best result if $y^+ < 5$.

Table 3.1.   Regions featured with different y⁺ values

Y plus value	Name of region	Feature
$y^+ < 5$	Viscous sublayer region	Velocity profiles are assumed to be laminar and viscous stress dominates the wall shear
$5 < y^+ < 30$	Buffer region	Both viscous and turbulent shear dominate
$30 < y^+ < 300$	Fully turbulent portion of log-law region	Turbulent shear predominates

3.1.5.   Turbulence Models

Turbulence model is one of the key features in air flow modelling, since it influences the accuracy of numerical simulation significantly. There are three turbulence models taken into consideration as candidates. They are Standard $k - \varepsilon$ Model, Realizable $k - \varepsilon$ Model and Reynolds Stress Model (RSM).

Standard k-ε Model

The Standard $k - \varepsilon$ Model is a semi-empirical turbulence model, which was proposed by Launder and Spalding [56]. It has been very popular due to the robustness, economy and reasonable accuracy for a wide range of turbulent flow problems. The

25

model is based on the turbulence kinetic energy (k) and its dissipation rate (ε), which are derived from exact equation and empirical reasoning respectively. In the Standard $k - \varepsilon$ Model, it is assumed that the flow is completely turbulent, and the effects of molecular viscosity are negligible. Hence, it is only applicable for fully turbulent flows.

Realizable k-ε Model

When the strain is large enough, Schwarz inequality of shear stresses get violated. To prevent such violations *i.e.* to guarantee the model is "realizable", it is necessary to consider the turbulent viscosity coefficient, C_μ, become dependent on the mean flow (mean deformation) and the turbulence (k, ε). Hence, two modifications have been done for Realizable $k - \varepsilon$ Model:

- There is an alternative formulation of turbulent viscosity, which includes C_μ.

- The transport equation of the dissipation rate, ε, is based on the dynamic equation of the mean-square vorticity fluctuation.

Initial studies show that Realizable $k - \varepsilon$ Model performs the best among all the $k - \varepsilon$ models, except that it produces non-physical turbulent viscosities when both rotating and stationary fluid zones are involved.

Reynolds Stress Model

The Reynolds Stress Model (RSM) has added seven transport equations to the 3D calculation. It is very popular for the simulations such as cyclone flows, combustor flows, rotating flow passages and the stress-induced secondary flows in duct, due to the superior performance to capture of swirl, rotation and rapid changes in strain rate. However, the fidelity is still limited by the employed assumptions, modeling of pressure-strain and dissipation rate, as well as the scale equations ($\varepsilon -$ or $\omega -$).

3.2. Numerical Model

3.2.1. Problem Statement

The geometry under study is the testbed described in the previous chapter. In order to adopt the inherited fan model of ANSYS FLUENT, a structured mesh with hexahedral elements is implemented. To fit in the structured mesh, the round-shaped cross-sections of the heater-fan, the inlet, and the outlet are converted to square-shaped cross-sections with the same surface areas, so that the flow rates do not change due to the shape changes. The heater-fan model includes a fan surface and a heat source volume, which provide sources for momentum and thermal energy, respectively. The dimension of the heat source is $2.36 \times 10^{-4}\ m^3$. The simulation version of the testbed is shown in Figure 3.3. The details of modification are given in Table 3.2.

The computation domain is limited to the interior of the testbed, without considering the interaction between the testbed and the surrounding lab environment. To account for heat transfer with the environment, the wall temperatures are measured in the experiments and assigned as boundary conditions in the numerical simulations.
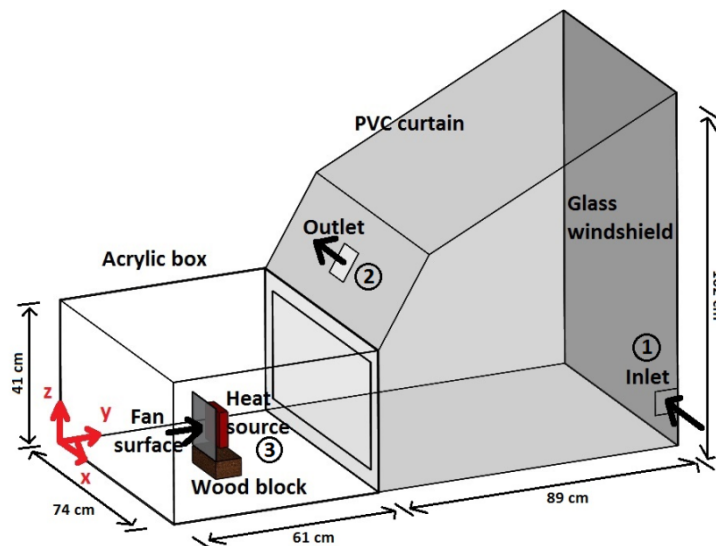
Figure 3.3. **The testbed model after modification: 1) Inlet; 2) Outlet; 3) Fan model**

Table 3.2.   Dimension modifications of testbed in numerical simulation

Component	Original dimension	Modified dimension
	cm	cm
Fan surface	Φ17	15×15
Inlet	Φ8	7×7
Outlet	Φ10	9×9

3.2.2.   Mesh Generation

The mesh is divided into two regions, the interior and the boundary (near-wall region). With the purpose of grid-dependency study, three levels of mesh refinement are applied for both regions. The mesh gets finer from 1 to 3 for both interior and boundary. The global elements size for *interior 1, interior 2 and interior 3* are 7.62, 5.08 and 2.54 cm, respectively. The heights of the first layer of mesh at the wall in each boundary type are 0.08, 0.25 and 1.27 cm, respectively. In addition, the mesh is refined around the fan area. The mesh sizes of different combinations with interior (global) and boundary types are given in Table 3.3.

Table 3.3.   Mesh size of different interior and boundary types

Mesh size	Interior 1	Interior 2	Interior 3
Boundary 1	30759	75998	218383
Boundary 2	85346	152774	306600
Boundary 3	211509	331928	520620

Three type of boundary mesh around the fan model are shown in Figure 3.4. The heights of the first layer element near wall are 0.762, 0.254 and 0.0762 cm (0.3, 0.1 and 0.03 inch), respectively. The y^+ values for these three boundary types are in viscous sublayer region, buffer region and log-law region, respectively.
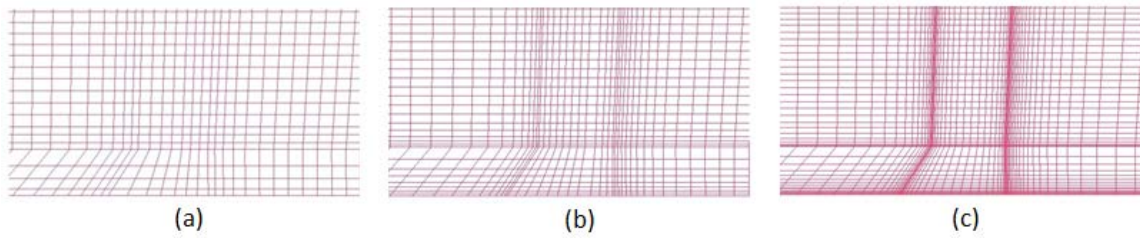
Figure 3.4. Demonstration of 3-level boundary types at near wall region: a cross-section around heater-fan

3.2.3. Boundary Conditions

The experiments of Chapter 2 provide the boundary conditions for the numerical simulation. In addition, a few calculations are required for the other input parameters in ANSYS FLUENT.

ANSYS FLUENT provides an inherited fan model. A fan is considered to be infinitely thin, and the discontinuous pressure rise across it is specified as a function of the velocity through the fan. The relationship may be a constant, a polynomial, piecewise-linear, or piecewise-polynomial function, or a user-defined function. In present study, a constant pressure is assigned in each scenario and the pressure jump is calculated via Bernoulli equation according to the measurement of experiment:

$$\Delta p = \frac{1}{2}\rho u^2 \tag{3.10}$$

where ρ is the air density, and u is air flow velocity. An average is taken for all wall temperatures and the inlet, and the values of ρ are assigned according to this average wall temperature for each case. The details are shown in Table 3.4.

Table 3.4. Surface fan model parameters

Tests	Average temperature	Air density	Fan velocity	Pressure jump
	°C	kg/m³	m/s	pa
Test 1	21	1.196	1.25	0.934375
Test 2	42	1.117	1.45	1.174246
Test 3	27	1.172	1.80	1.898640
Test 4	21	1.196	0.98	0.574319

In ANSYS FLUENT, the heat source is defined in watt per cubic metre. The conversion is given in Table 3.5.

Table 3.5.   Heat source conversion

Tests	Heater power	Heat source volume	Heat source term defined in ANSYS FLUENT
	W	m^3	W/m^3
Test 1	529.21	2.36×10^{-4}	2242415
Test 2	600.00	2.36×10^{-4}	2542373
Test 3	746.38	2.36×10^{-4}	3162627
Test 4	390.71	2.36×10^{-4}	1655551

3.3. Results and Discussion

Numerical simulations corresponding to the experimental tests are performed with three different turbulence models and 9 different meshes. Non-Equilibrium Wall Functions are implemented for all. The simulations are regarded as converged when the residuals reach to 10^{-3} or smaller values. All the turbulence models converge with second order upwind.

The velocity magnitude of the experiment is in a certain range that the natural convection is negligible. Therefore, natural convection term is not turned on in ANSYS FLUENT simulations.

3.3.1.   Grid-dependency Study over Interior Mesh

Grid-dependency check is performed for interior mesh type. The results from realizable $k - \varepsilon$ model are taken as examples in this section. Figure 3.5 shows the comparison of *test 1* between the experiments and numerical results with *boundary 3* but different interior (global) element sizes.

The numerical simulation values don't show significant difference among the chosen different maximum element sizes. To avoid further increase of aspect ratio,

which decreases the mesh quality and simulation accuracy, bigger mesh sizes are not tested.
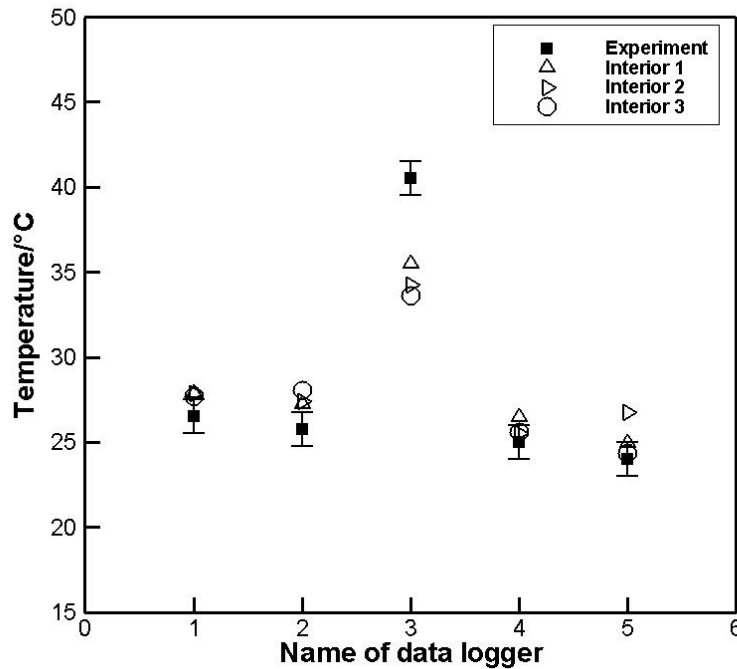
Figure 3.5. **Comparison of experiment and numerical simulations for temperature: different interior element size**

3.3.2. Grid-dependency Study over Boundary Mesh

Another set of grid-dependency check is performed for boundary mesh type. The result from realizable $k - \varepsilon$ model is shown in Figure 3.6, which is the comparison between the experiments and numerical results for *test 1* with *interior 3* but different boundary layer type.

In contrast to the comparison among different interior mesh, the numerical simulation values show significant different among different boundary mesh type. When the y+ value is in the viscous sub-layer region, the numerical simulation gives the best agreement with the experimental data, which is in accordance with the conclusion of the literatures.
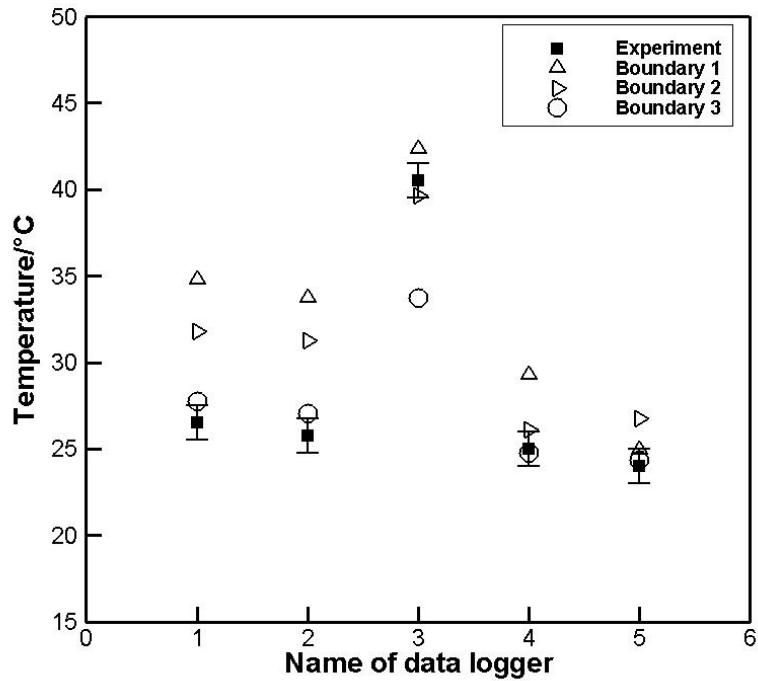
Figure 3.6. Comparison of experiment and numerical simulations for temperature: different boundary element size

3.3.3. *Performance of Turbulence Models*

Numerical simulations are conducted with different turbulence models for *test 1 to test 4*. The mesh type is *interior 3 + boundary 3* for all. The comparisons between experimental and numerical results are given in Figure 3.7 to Figure 3.10.

It can be concluded from the comparison that realizable $k - \varepsilon$ gives the best agreement, except the third data logger results. Therefore, sensitivity analysis is done for the position of data loggers in the next subsection.
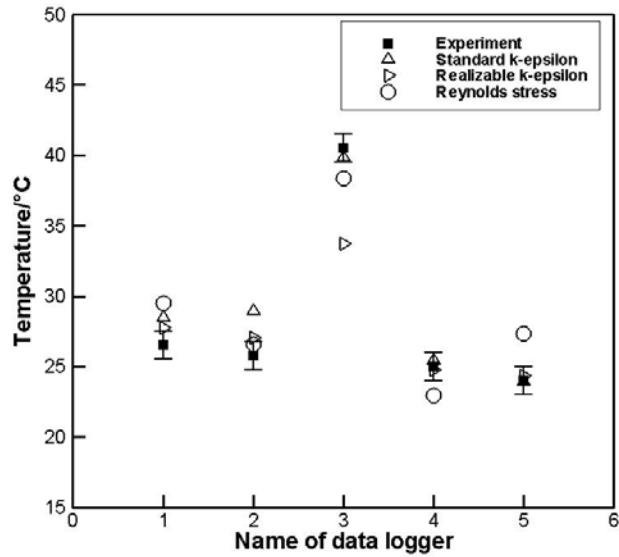
Figure 3.7. Comparison of experiment and numerical simulations for temperature: different turbulence model; Test 1
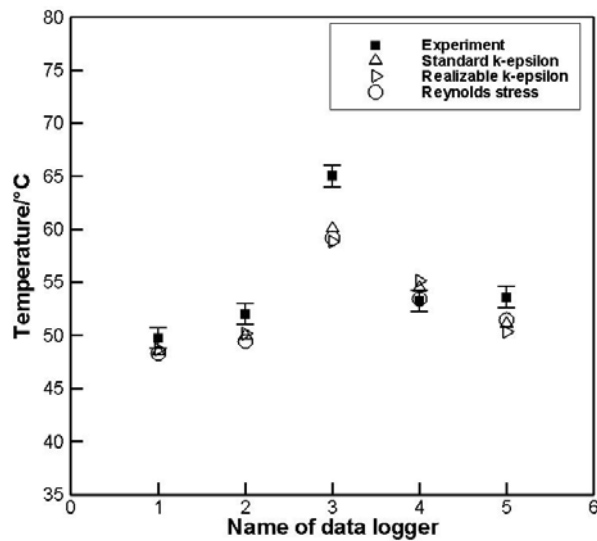
Figure 3.8. Comparison of experiment and numerical simulations for temperature: different turbulence model; Test 2
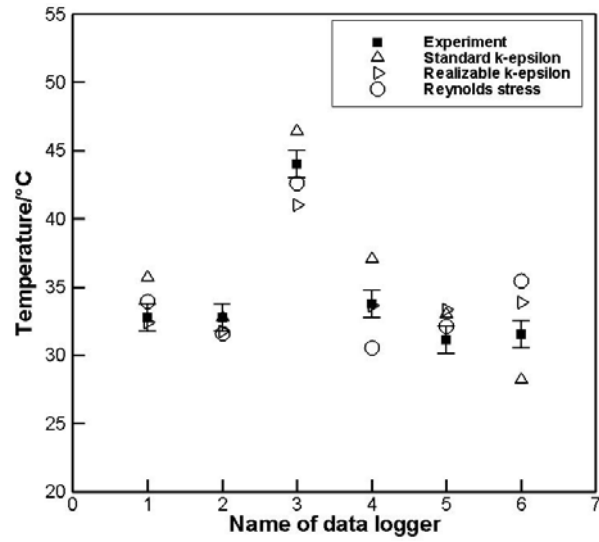
Figure 3.9. Comparison of experiment and numerical simulations for temperature: different turbulence model; Test 3
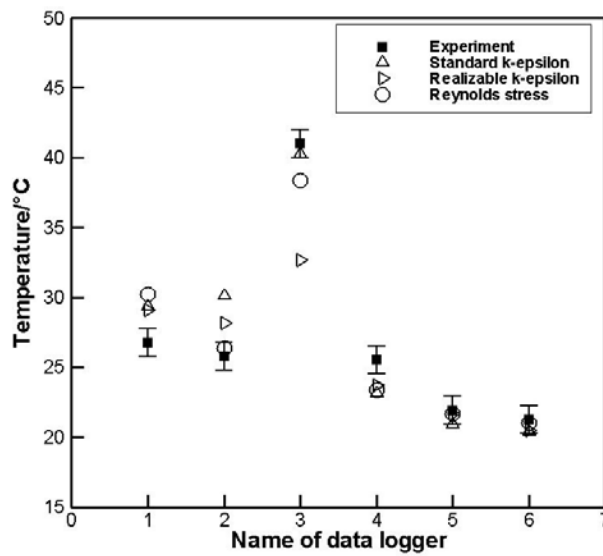
Figure 3.10. Comparison of experiment and numerical simulations for temperature: different turbulence model; Test 4

3.3.4.   Sensitivity Analysis

To evaluate the sensitivity of the temperature magnitude at each point in numerical simulation, virtual spheres with 2 cm radius are assumed, with the original measuring points as centres. Extra six points are taken, for each original measuring point, at the surface of the sphere along the 3 coordinates. The result in Figure 3.11 shows that the largest deviation among the temperatures of adjacent points is 8°C for data logger 3, 5°C for data logger 5, and no more than 2°C for the others. This result explains the large deviation between the experimental and numerical results at the position of data logger 3. The model is inaccurate in this region, so we won't take measurement in this region.
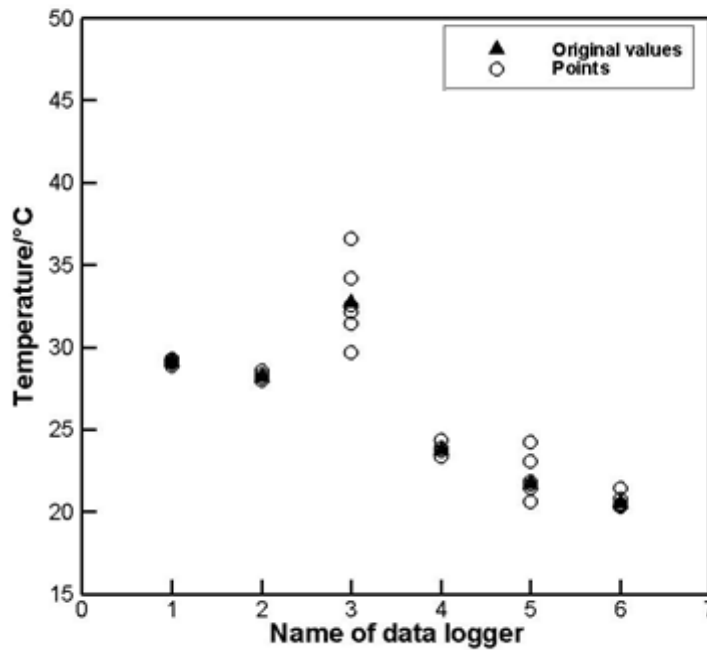
Figure 3.11.   Temperature sensitivity analysis of adjacent points

3.4. Conclusions

A comprehensive and systematic numerical study is performed to regenerate the experimental data of Chapter 2 and select the turbulence model, and mesh structure. A

few modifications are implemented on geometry to fit in the requirements of numerical simulation.

Grid-dependency check shows that the mesh type (size) of boundary layer plays a significant role in the performance of simulation while the far-wall mesh doesn't. When the y^+ value is in the range of viscous sublayer region, the best simulation accuracy is obtained.

Standard $k-\varepsilon$ Model, Realizable $k-\varepsilon$ Model and Reynolds Stress Model (RSM) are compared as candidates. As a result, Realizable $k-\varepsilon$ Model stands out with its superior accuracy.

The above conclusion is implemented to the following chapter for the thermal comfort study in vehicle cabin.

Chapter 4.

Numerical Simulation of Vehicle Cabin

The previous chapter confirms that Realizable $k-\varepsilon$ Model shows the best agreement with the experimental results when the near-wall mesh satisfy $y^+ < 5$. To investigate and optimize the air flow system inside the eVaro model, and the above conclusion is implemented. This newly developed hybrid vehicle model has a shape originated from fighter jet for aerodynamics and stability. It should be noted that there are only two seats, which is different from the conventional vehicle models. In the following paragraphs, the study of air flow distribution inside the cabin is discussed. The geometry, mesh and boundary condition settings are described in details. The effect of different inlet and outlet arrangements are compared according to the numerical simulation results in the final subsection.

4.1. Numerical Model

4.1.1. Problem Statement

The SolidWorks model of the eVaro inner geometry is shown in Figure 4.1, which is built according to the 3D scanning data. A good geometry for numerical simulation should capture as much detail as possible while not lowering the mesh quality. To achieve this, the geometry is processed in two levels, SolidWorks and ICEM CFD.
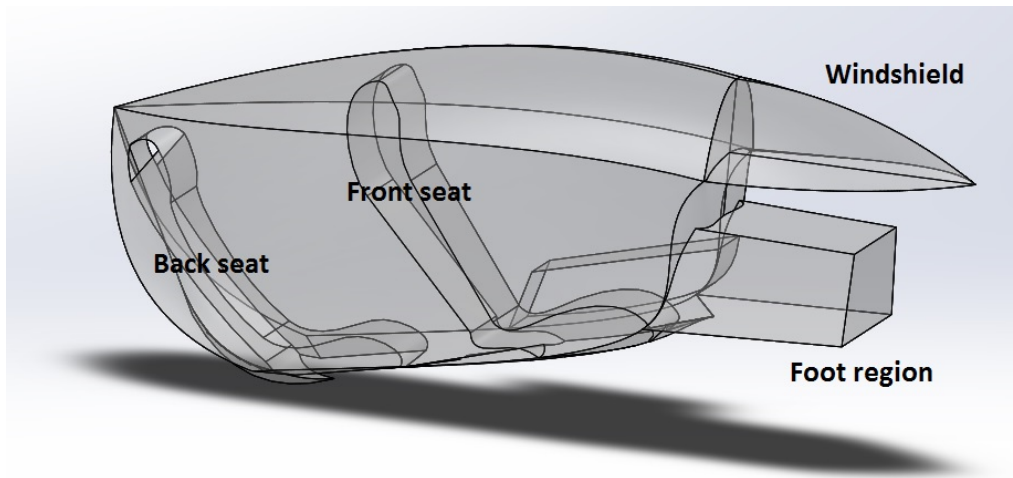
Figure 4.1.   The SolidWorks model of the eVaro inner geometry

It has been noticed from preliminary meshing that the low-quality grids come from sharp angles between structural faces and lines (as highlighted in Figure 4.2). At the SolidWorks level (Figure 4.3), the sharp corner between windshield and the bottom board is handled simply by applying fillet; the sharp junctions between the seats and the bottom wall of the cabin are removed with round-shape cut-extrusion due to their complexity.

At ICEM CFD level, surface boundary lines with sharp angles are removed. The meshing process captures structural element in the order of point, curve and surface. Hence, the mesh will capture surface instead of the sharp angle between lines when they are removed.

Despite the above mentioned modification, numerous extrusions are added at the locations of vents in SolidWorks. These extruded parts are removed and the interfaces are modified into regular vents in ICEM CFD (Figure 4.4).
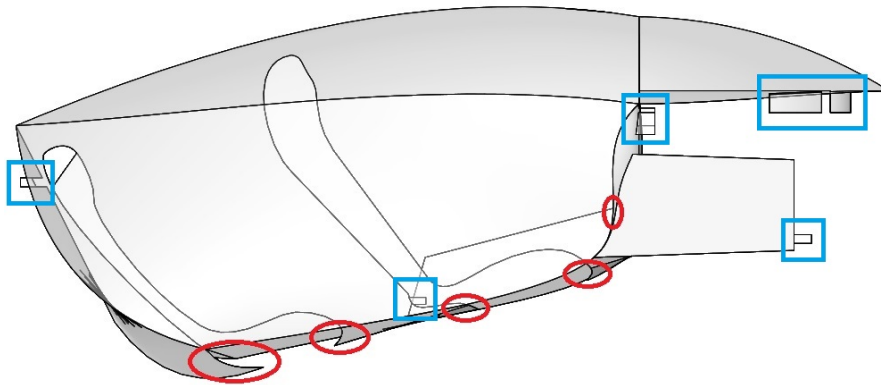
Figure 4.2.   The eVaro geometry: The indication of modification-required parts
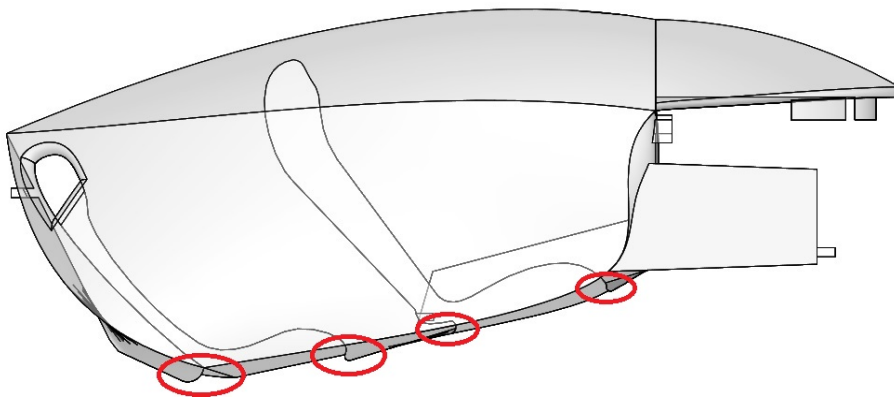
Figure 4.3.   The eVaro geometry: After modification in SolidWorks
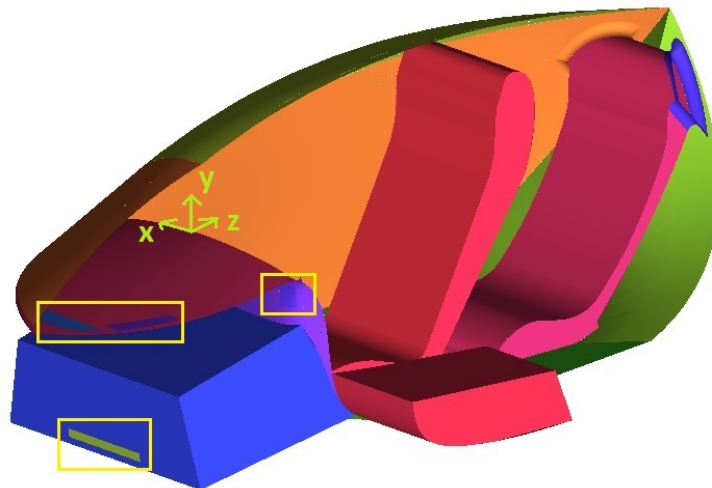
Figure 4.4.   The eVaro geometry in ICEM: The vent-extrusions are cleaned up

4.1.2. Mesh Generation

A mesh could be generated in a way that more than 90% of it is structured. However, this type of mesh is not eligible for the treatment of quality improvement in ICEM CFD, which is a critical process of mesh generation. Considering that the far-wall mesh is proved to affect the simulation accuracy less and a prism layer, which is in more regular shape, is built at the boundary, an unstructured mesh is implemented for the eVaro cabin model. The mesh is set to automatically capture the curves with finer grids according to the radians. In addition, finer mesh is used for the surface of vents. There are three layer of prism mesh at the boundary, in order to satisfy $y^+ < 5$, which provides better simulation accuracy according to the study of previous section. (Please refer to Figure 4.5)

The original point for the geometry is set at the mid-point of the interface between the surface under windshield and panel, as shown in Figure 4.4. It shows that the mesh size is dominated by the curvature based refinement rather than the global element size. Two lines at the driver seat region are taken to compare the temperature for grid-dependency study. One is from (-0.35, 0, 0.4) to (0.35, 0, 40) in meter; the other is from (0, 0.1, -0.3) to (0, 0.1, 0.6) in meter. The mesh sizes are given in Table 4.1. Grid-dependency check results are shown in Figure 4.6 and Figure 4.7. The temperature differences are no more than 1°C for the first line, and no more than 3°C for the second line. Therefore, Mesh 2 is chosen for further study.

Table 4.1.   The details of grid dependency study meshes

Features	Mesh size	Global element size	Curvature based refinement
		cm	cm
Mesh 1	319,277	7.62	0.508
Mesh 2	250,072	10.16	0.508
Mesh 3	249,314	12.7	0.508
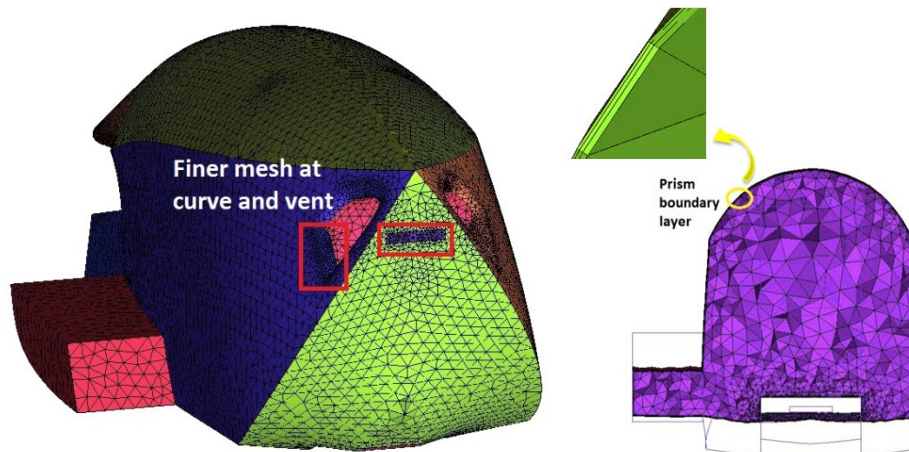
Figure 4.5. Mesh treatment: Finer mesh at curves and vents, and prism layer at boundary
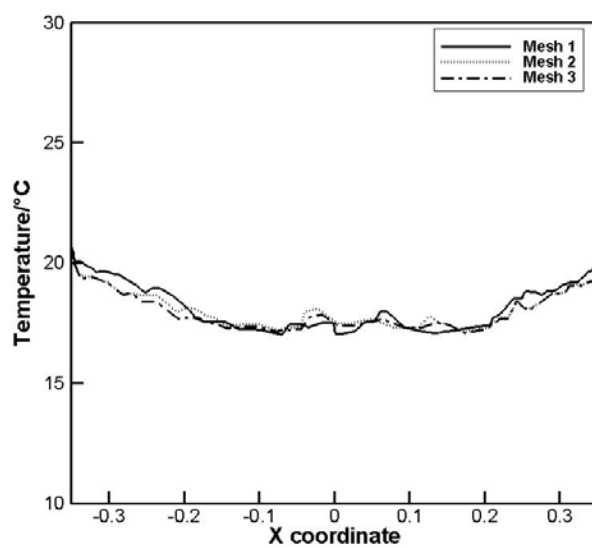
Figure 4.6. Grid dependency check: a line along x-coordinate, from (-0.35, 0, 0.4) to (0.35, 0, 0.4)
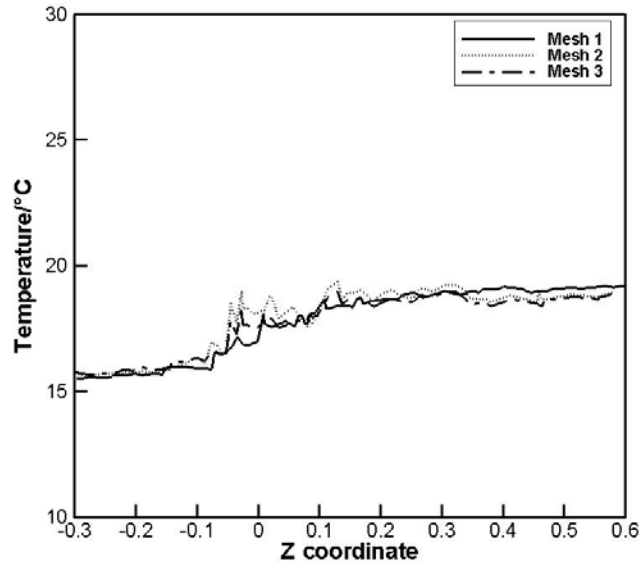
Figure 4.7. Grid dependency check: a line along z-coordinate, from (0, 0.1, -0.3) to (0, 0.1, 0.6)

4.1.3. Boundary Conditions

Inlets are located under the windshield, on the panel, on the rear surface of driver seat and on the side wall of passenger seat region. Outlets are arranged at the front surface of foot region and behind the passenger seat, as shown in Figure 4.8. The velocity inlet boundary condition is applied to the incoming flow vents, and pressure outlet boundary condition is applied to the outgoing flow vents. The surface boundary conditions are set according to [18], [53]–[55], which are considered as the worst case scenario. Top, right, left and rear surfaces of the cabin as well as the windshield are assigned with constant heat flux, while the other surfaces are designated with constant temperatures, as shown in Table 4.2.
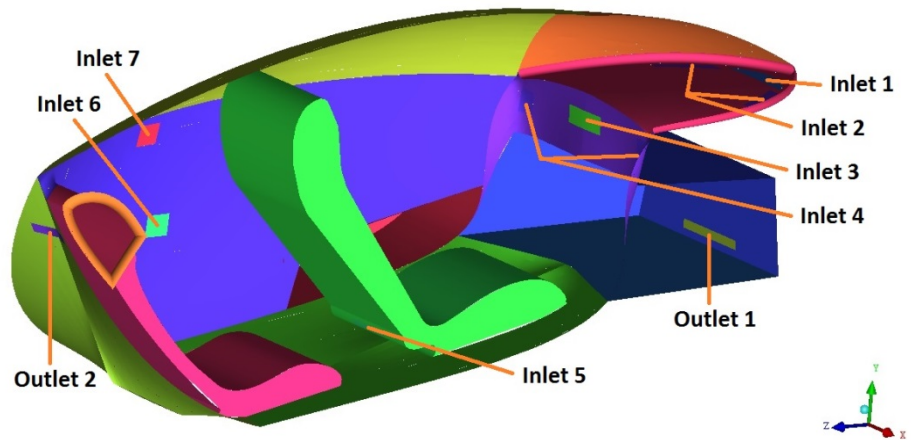
Figure 4.8.   The locations of inlets and outlets

Table 4.2.   The setting of boundary conditions

Name of component	Temperature	Heat leakage
	°C	W/m²
Windshield	--	385
Surface under the windshield	35	--
Top surface	--	30
Bottom surface	22	--
Right surface	--	30
Left surface	--	30
Rear surface	--	30
Panel	35	--
Top and side surfaces at foot region	35	--
Bottom surface at foot region	22	--
Front surface of front seat	22	--
Rear surface of front seat	22	--
Front surface of rear seat	22	--
Rear surface of rear seat	22	--
Cube beside left surface	22	--

4.1.4. Thermal Comfort Criteria

In the past few decades, researchers have proposed many techniques to evaluate thermal comfort. One of the indices that stand out as international standards is Predicted Mean Value (PMV). In ASHRAE, PMV is defined as an index that predicts the mean value of the votes of a large group of persons on the 7-point thermal sensation scale (Table 4.3), based on the heat balance of the human body. It provides criteria for comfort level, and can be calculated from Eqs. (4.1)-(4.4).

Table 4.3.   Seven-point thermal sensation scale

+3	Hot
+2	Warm
+1	Slightly warm
0	Neutral
-1	Slightly cool
-2	Cool
-3	Cold

$$PMV = \left[0.303 \cdot \exp(-0.036 \cdot M) + 0.028 \right]$$

$$\left\{ \begin{array}{l} (M-W) - 3.05 \times 10^{-3} \cdot \left[5.733 - 6.99 \cdot (M-W) - p_a \right] - 0.42 \cdot \left[(M-W) - 58.15 \right] \\ -1.7 \times 10^{-5} \cdot M \cdot (5867 - p_a) - 0.0014 \cdot M \cdot (34 - t_a) \\ -3.96 \times 10^{-8} \cdot f_{cl} \cdot \left[(t_{cl} + 273)^4 - (\overline{t_r} + 273)^4 \right] - f_{cl} \cdot h_c \cdot (t_{cl} - t_a) \end{array} \right\} \qquad (4.1)$$

$$t_{cl} =$$
$$35.7 - 0.028 \cdot (M-W) - I_{cl} \cdot \left\{ 3.96 \times 10^{-8} \cdot f_{cl} \cdot \left[(t_{cl} + 273)^4 - (\overline{t_r} + 273)^4 \right] + f_{cl} \cdot h_c \cdot (t_{cl} - t_a) \right\} \qquad (4.2)$$

$$h_c = \begin{cases} 2.38 \cdot |t_{cl} - t_a|^{0.25} & \text{for} \quad 2.38 \cdot |t_{cl} - t_a|^{0.25} > 12.1 \cdot \sqrt{v_{ar}} \\ 12.1 \cdot \sqrt{v_{ar}} & \text{for} \quad 2.38 \cdot |t_{cl} - t_a|^{0.25} < 12.1 \cdot \sqrt{v_{ar}} \end{cases} \qquad (4.3)$$

$$f_{cl} = \begin{cases} 1.00 + 1.290 l_{cl} & \text{for} \quad l_{cl} \le 0.078 m^2 \cdot K / W \\ 1.05 + 0.645 l_{cl} & \text{for} \quad l_{cl} > 0.078 m^2 \cdot K / W \end{cases} \qquad (4.4)$$

where, M is metabolic rate, W/m^2; W is the effective mechanical power, W/m^2; I_{cl} is clothing insulation, $m^2 \cdot K/W$; f_{cl} is the clothing surface area factor; t_a is the air temperature, $°C$; $\overline{t_r}$ is the mean radiant temperature, $°C$; v_{ar} is the relative air velocity, m/s; p_a is the vapour pressure of water, Pa; h_c is the convective heat transfer coefficient, $W/(m^2 \cdot K)$; t_{cl} is the clothing surface temperature, $°C$. Note that, 1 metabolic unit $=1$ met $=58.2W/m^2$; 1 clothing unit $=1$ clo $=0.155m^2 \cdot °C/W$.

The index should be used only for values of PMV between -2 and +2, and when the six main parameters are within the following intervals:

M $46W/m^2$ to $232W/m^2 (0.8 \text{ met to } 4 \text{ met})$;

I_{cl} $0m^2 \cdot K/W$ to $0.310m^2 \cdot K/W (0 \text{ clo to } 2 \text{ clo})$;

t_a $10°C$ to $30°C$;

$\overline{t_r}$ $10°C$ to $40°C$;

v_{ar} $0m/s$ to $1m/s$;

p_a $0Pa$ to $2700Pa$.

This parameter is used to evaluate the simulation results in the following subsections.

4.1.5. User Defined Function (UDF)

User Defined Function (UDF) is a special type of code written in C language. It is an extension to the inherent functions ANSYS FLUENT has, and helps to execute additional commands. The specifications for each command can be referred to the ANSYS HELP document [57].

For the purpose of calculating the Predicted Mean Value (PMV) index, an ON_DEMAND UDF is written and interpreted to the numerical simulation of vehicle cabin. This UDF outputs PMV value by combining the given clothing, metabolic rate, radiation, and humidity conditions with the temperature and velocity parameters, which are extracted from ANSYS FLUENT. In the cooling scenarios, the humidity is assumed to be 50 %, the radiation temperature (environment temperature) is 35°C, clothing is 1 unit, metabolic rate is 1 unit, and external work is 0. Refer to Appendix A for details of the UDF.

4.2. Results and Discussions

The results of different ventilation arrangements are compared to each other in this section. The thermal comfort level of the driver seat region and passenger seat region are discussed according to PMV index, which is defined in the previous subsection.

4.2.1. *Thermal Comfort of Driver Seat Region*

Seven scenarios are tested for the thermal comfort level of the driver seat region. According to the definition of PMV, the velocity is required to be in the range of 0~1 m/s. Therefore, the inlets on the panel are assigned with a velocity of 1 m/s, while the inlets under the windshield are designated with a velocity of 2 m/s. The velocity decreases to 1m/s when the air flow from windshield reaches driver seat region. To evaluate the performance of each vent in the vehicle cabin, some vents are sealed and set to wall boundary condition in some scenarios. The specifications are given in Table 4.4.

The simulations are regarded as converged when the residuals reach 1×10^{-3}. The UDF is interpreted and executed in ANSYS FLUENT. The PMV contours are displayed via two cut planes. They are mid$-y-z$ plane and $z-x$ plane at $z = -15$, which is at the level of driver's chest.

Effect of Outlet Locations

To examine the effect of outlet locations, both windshield and side panel inlets are open in Test 1~3. The details are shown in Table 4.4, where the sealed vents are not mentioned. They differ from each other with different outlets arrangement. When only the rear outlet is open (Figure 4.9), the PMV value tends to be high at driver's chest and foot region. When both outlets are open (Figure 4.10), the driver seat region keeps a better thermal comfort level, and it turns slightly better when the rear outlet is blocked (Figure 4.11). Therefore, it can be concluded that the front outlet plays a significant role in the thermal comfort of the driver.

Table 4.4.   Test design for the study of driver-seat thermal comfort: outlets

Component	Location	Test scenario		
		1	2	3
		Inlet velocity		
		m/s		
Inlet 1	Under the windshield	2	2	2
Inlet 2	Under the windshield	2	2	2
Inlet 4	On the panel (side)	1	1	1
Outlet 1	In the foot region	--	Open	Open
Outlet 2	Behind the rear seat	Open	Open	--

Figure 4.9.   PMV contour: Test 1

Figure 4.10.   PMV contour: Test 2

Figure 4.11.   PMV contour: Test 3

Effect of Inlet Locations

In order to examine the effect of inlet locations, four more scenarios are simulated, taking Test 3 (Figure 4.11) as comparison. The details of the setting are shown in Table 4.5, where the sealed vents are not mentioned.   Different inlet arrangements are applied while the total inlet air flow rate is constant. When both the panel inlets are blocked (Test 4, Figure 4.12), the driver's head region tends to be cold and the chest region tends to be hot. When the second windshield are blocked (Test 5, Figure 4.13 and Test 6, Figure 4.14), the driver's seat region turns hot and the chest region tends to be cold. When the inlet velocity is decreased (Test 7, Figure 4.15), the windshield air flow fails to provide air curtain along the top surface of the vehicle cabin, and it is also disturbed by middle panel inlet flow.

As a conclusion, the windshield air flow plays a significant role for the thermal comfort of driver, and the inlet velocity has to be kept at no less than 2 m/s to ensure the

48

air flow curtain along the top surface of the cabin; the middle panel inlet flow disturbs the windshield inlet flow, therefore, only side panel inlets are suggested.

Table 4.5.   Test design for the study of driver-seat thermal comfort: Inlets

Component	Location	Surface area	Test scenario				
		cm^2	3	4	5	6	7
Inlet 1	Under the windshield	105.1	2	2.3	2	2	1.5
Inlet 2	Under the windshield	133.7	2	2.3	--	--	1.5
Inlet 3	On the panel (middle)	77.5	--	--	--	2.3	1.3
Inlet 4	On the panel (side)	66.4	1	--	5	2.3	1.3
Outlet 1	In the foot region	46.5	Open	Open	Open	Open	Open
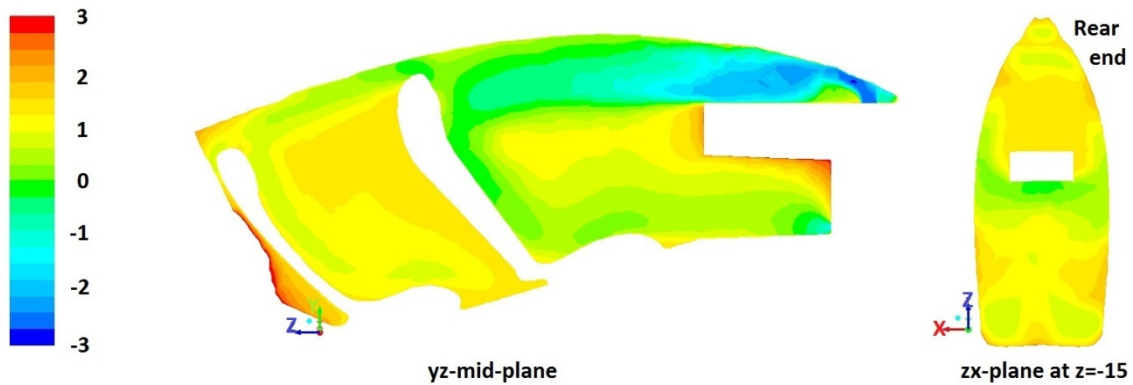
Figure 4.12.   PMV contour: Test 4
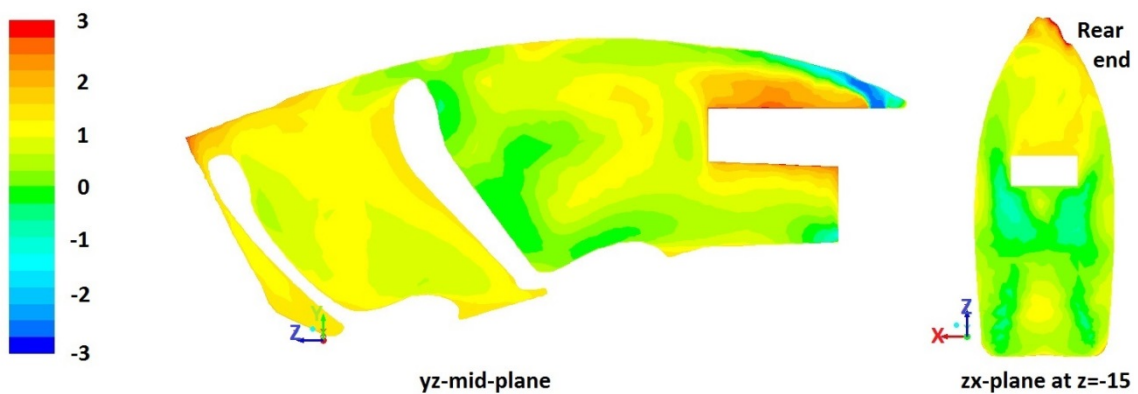
Figure 4.13.   PMV contour: Test 5
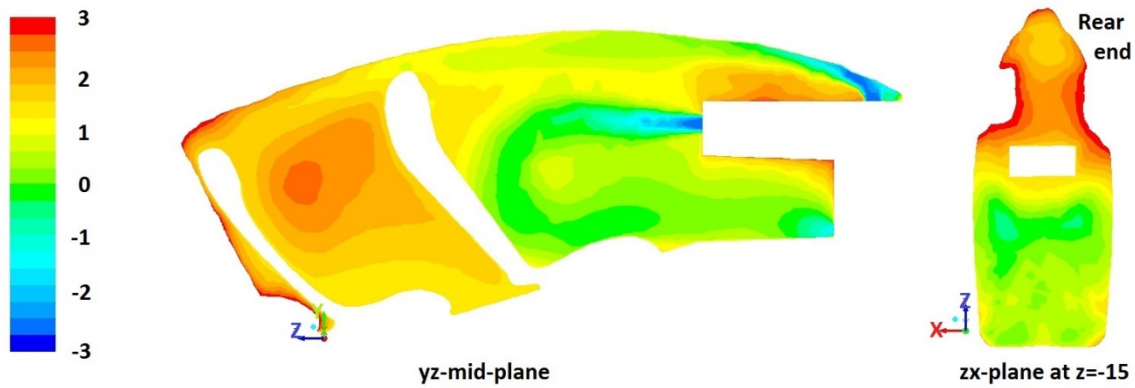
Figure 4.14.   PMV contour: Test 6
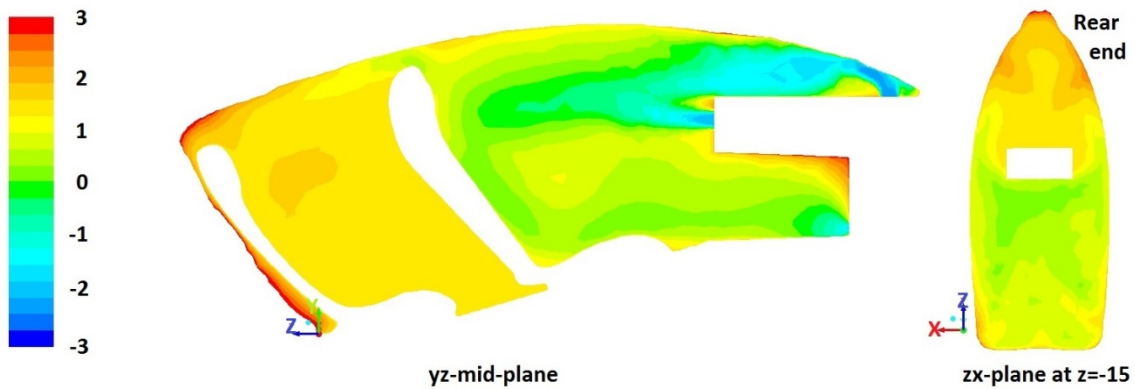
Figure 4.15.   PMV contour: Test 7

4.2.2.   Thermal Comfort of Passenger Seat Region

More scenarios are tested for the thermal comfort level of the passenger seat region. The settings of windshield inlets, panel inlet and front outlet followed the result from previous subsection. Three inlet vents and rear outlet are investigated for the purpose of passenger seat thermal comfort. In each scenario, different combinations of vents are evaluated.

The simulations are regarded as converged when the residuals reach 10^{-3}. The UDF is interpreted and executed in ANSYS FLUENT. The PMV contours are displayed via two cut planes. They are mid$-y-z$ plane and $z-x$ plane at $z=-30$, which is at the level of passenger's chest.

Effect of Outlet Locations

To examine the necessity of rear outlet, simulations are conducted when the rear outlet is open and sealed. The details are shown in Table 4.6, where the sealed vents are not mentioned. They differ from each other with different outlets arrangement. The case with the rear outlet open (Figure 4.17) shows a better thermal comfort level than the one with the rear outlet sealed (Figure 4.16).

Table 4.6.   Test design for the study of passenger-seat thermal comfort: outlet

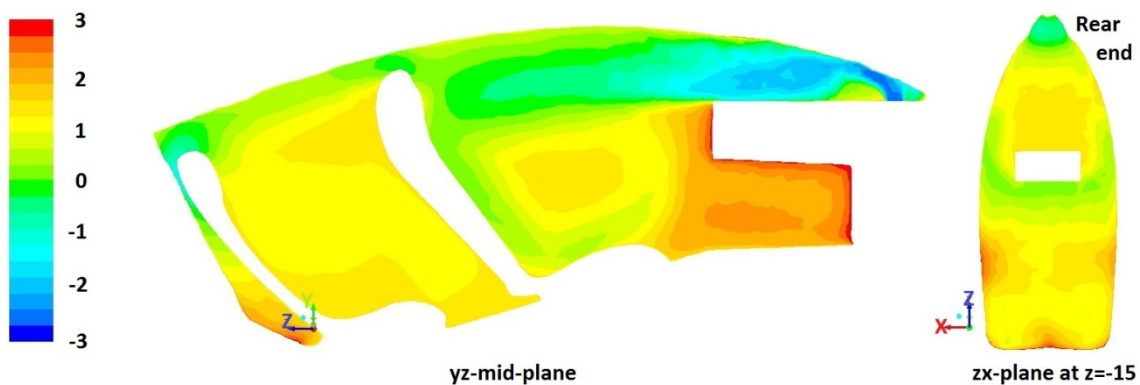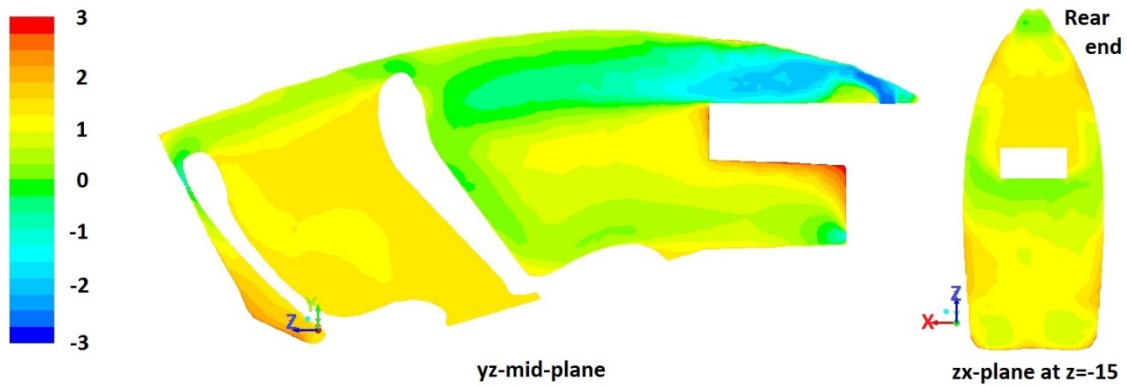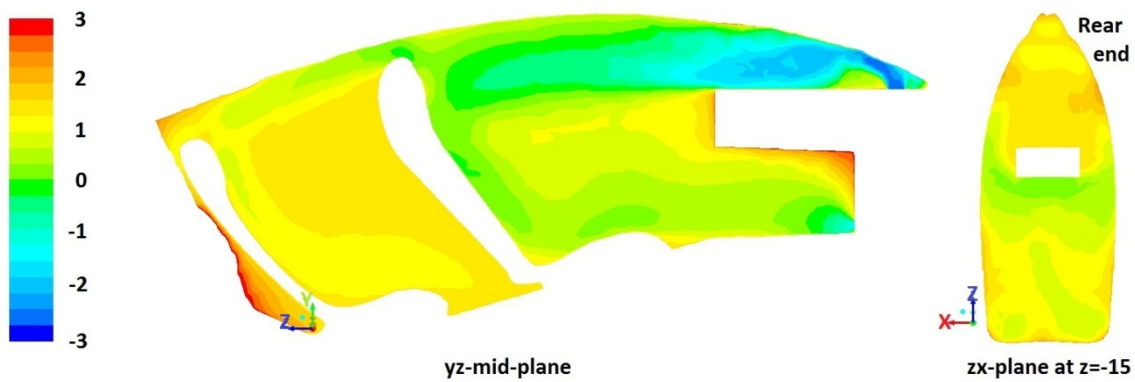| | | Test scenario | |
		8	9
Component	Location	Inlet velocity	
		m/s	
Inlet 1	Under the windshield	2	2
Inlet 2	Under the windshield	2	2
Inlet 4	On the panel (side)	1	1
Inlet 5	Behind the front seat	2	2
Outlet 1	In the foot region	--	Open
Outlet 2	Behind the rear seat	Open	Open
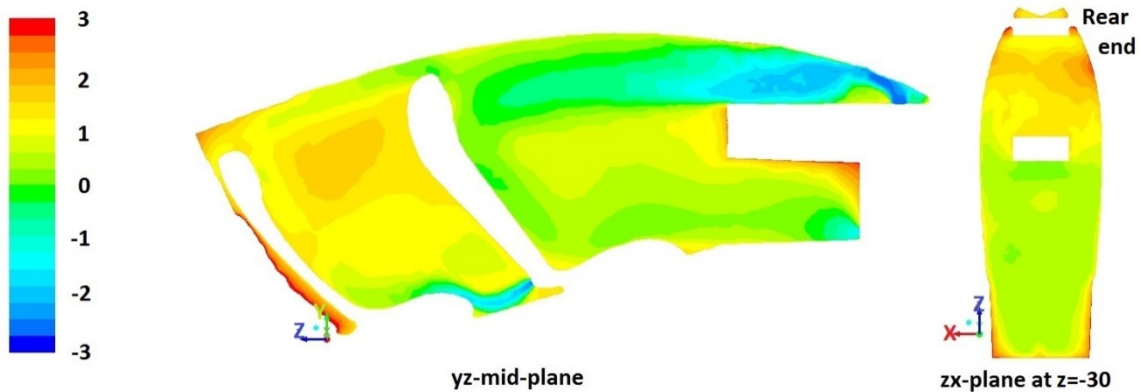
Figure 4.16.   PMV contour: Test 8
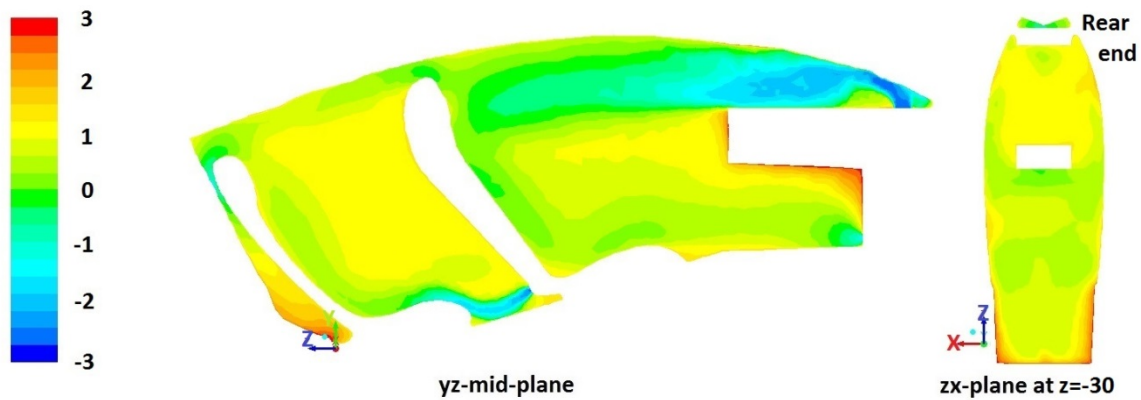
Figure 4.17. PMV contour: Test 9

Effect of Inlet Locations

In order to examine the effect of inlet locations, more scenarios are simulated. There are three sets of inlets and different combinations are applied while the total inlet air flow rate is constant, as indicated in Table 4.7. The velocity directions are vertical to the inlet surfaces. When either of the Inlet 6 or Inlet 7 is blocked, the PMV contour becomes more non-uniform (Figure 4.19a and Figure 4.20a). When Inlet 5, Inlet 6 or Inlet 7 operates alone (Figure 4.22, Figure 4.23 and Figure 4.24), the cases become even less comfortable. When all of the three inlets are open (Figure 4.18a) or only Inlet 5 is blocked (Figure 4.21a), the PMV contour is relatively more uniform and doesn't show significant difference from each other. Considering that passenger's feet can block Inlet 5, Test 13 is regarded as a better option.

However, when the air flow rate is increased by 50% (Figure 4.18b, Figure 4.19b, Figure 4.20b and Figure 4.21b), the comfort level only changes for local region rather than the entire passenger region. To improve the situation, the direction of inlet velocity is investigated in the next subsection.

Table 4.7.   Test design for the study of passenger-seat thermal comfort: inlets

Component	Location	Surface area	Test scenario						
		cm²	10	11	12	13	14	15	16
Inlet 1	Under the windshield	105.1	2	2	2	2	2	2	2
Inlet 2	Under the windshield	133.7	2	2	2	2	2	2	2
Inlet 4	On the panel (side)	66.4	1	1	1	1	1	1	1
Inlet 5	Behind the front seat	36.6	1	1.8	1.7	--	6.5	--	--
Inlet 6	On the side wall (middle)	97.4	1	1.8	--	1.2	--	2.4	--
Inlet 7	On the side wall (top)	102.9	1	--	1.7	1.2	--	--	2.3
Outlet 1	In the foot region	46.5	Open	Open	Open	Open	Open	Open	Open
Outlet 2	Behind the rear seat	64.5	Open	Open	Open	Open	Open	Open	Open

yz-mid-plane

zx-plane at z=-30

(a)

yz-mid-plane

zx-plane at z=-30

(b)
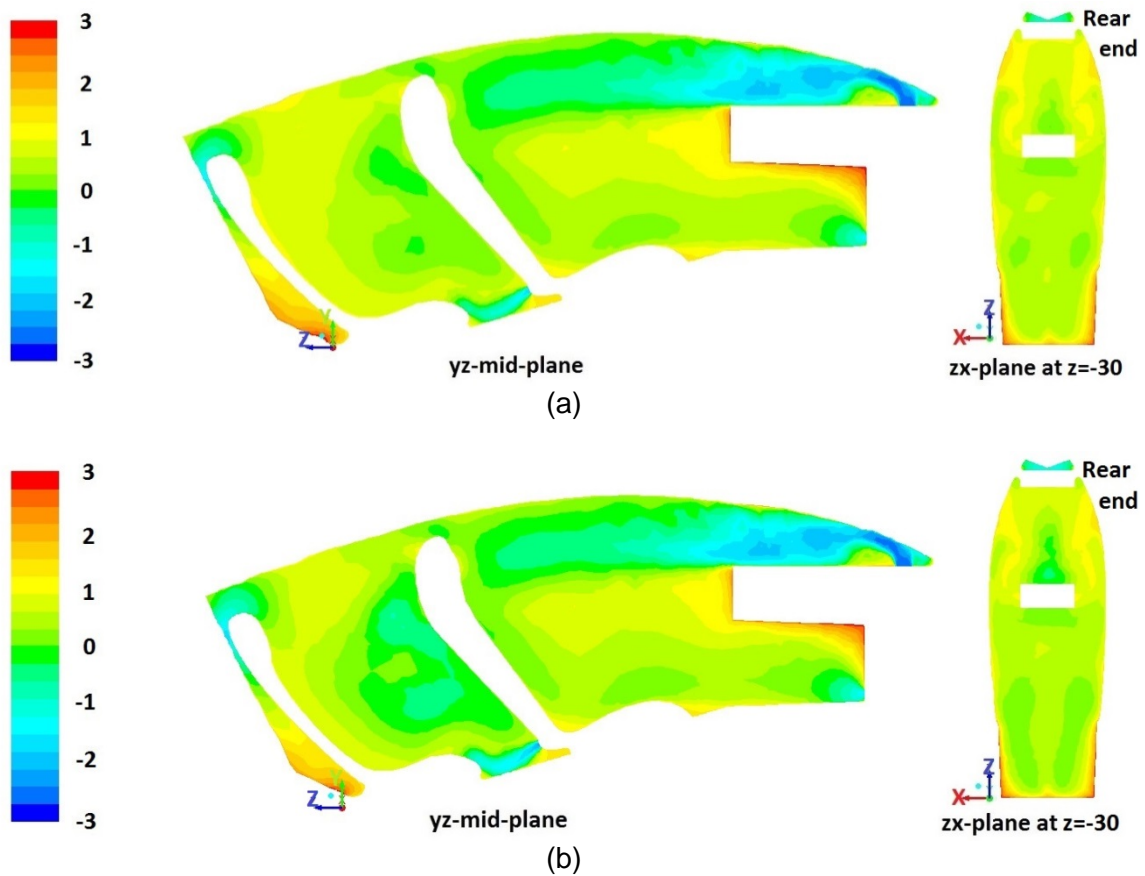
Figure 4.18.   PMV contour: (a) Test 10; (b) Test 17

yz-mid-plane

zx-plane at z=-30

(a)

yz-mid-plane

zx-plane at z=-30

(b)
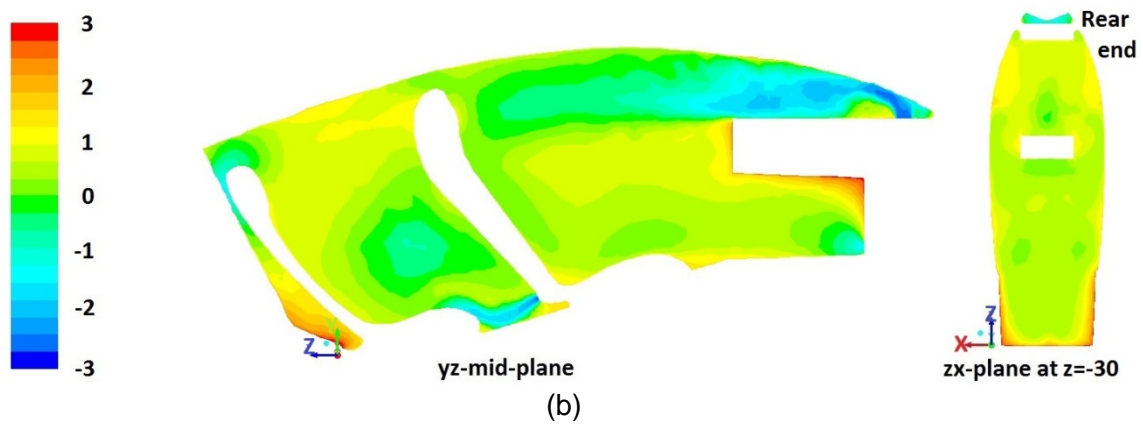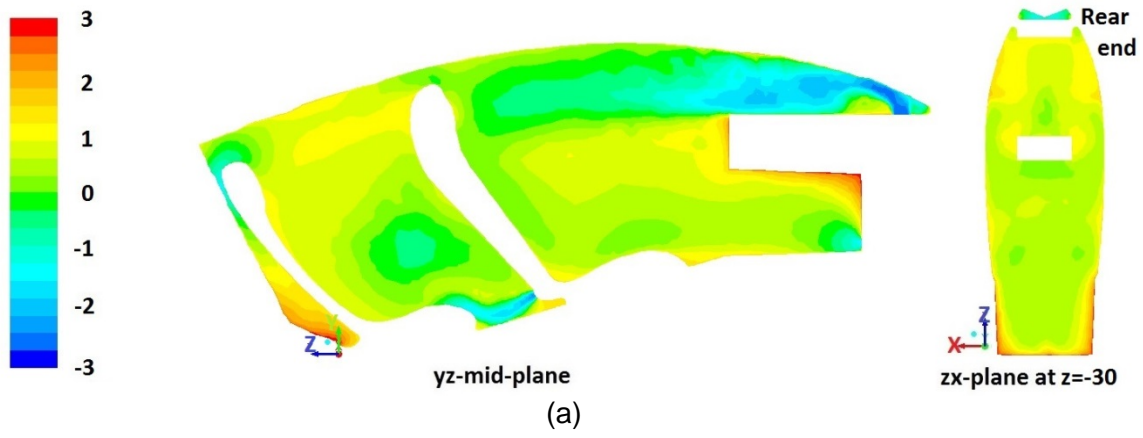
Figure 4.19.   PMV contour: (a) Test 11; (b) Test 18

yz-mid-plane

zx-plane at z=-30

(a)

Figure 4.20. PMV contour: (a) Test 12; (b) Test 19

**Figure 4.21.** PMV contour: (a) Test 13; (b) Test 20
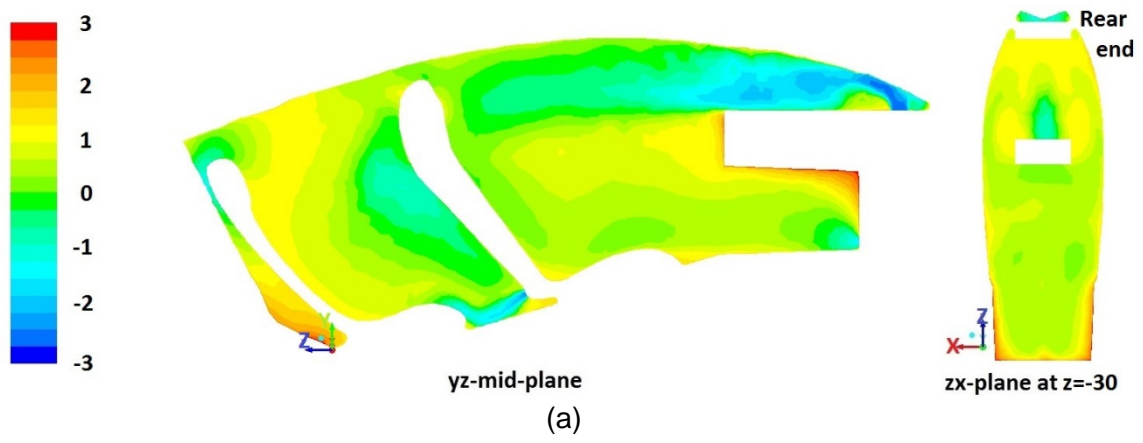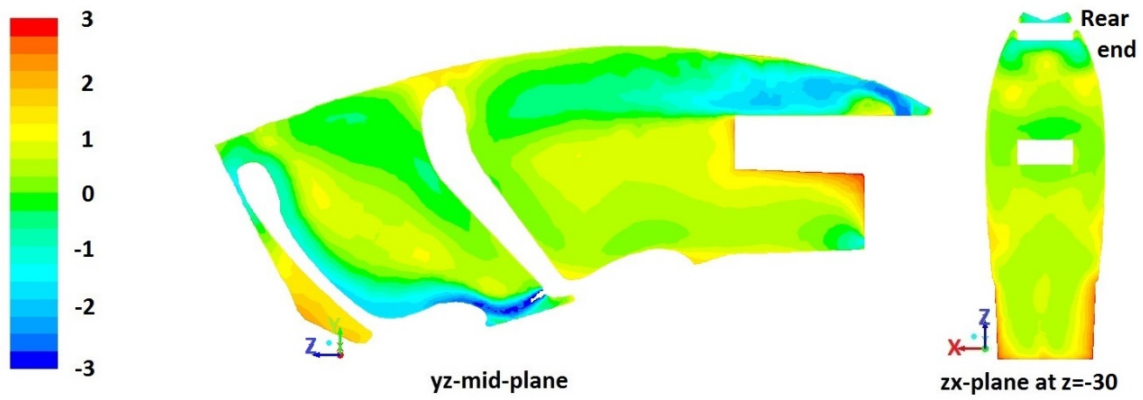
Figure 4.22.   PMV contour: Test 14
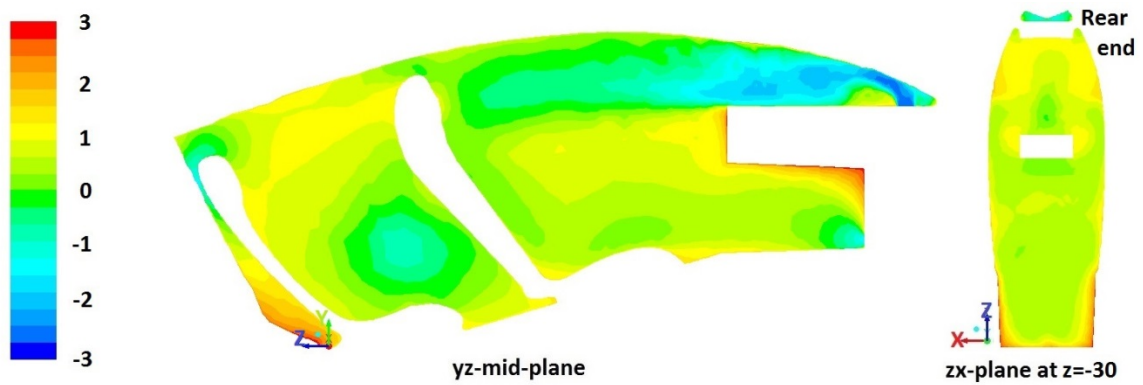
Figure 4.23.   PMV contour: Test 15
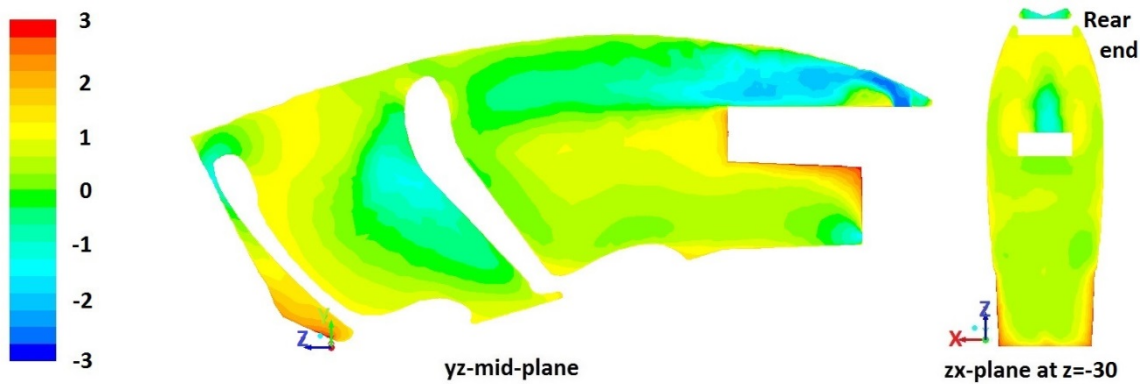
Figure 4.24.   PMV contour: Test 16

Effect of Horizontal Velocity Direction

To investigate the effect of horizontal velocity direction, three scenarios are tested with the air flow rate is increased by 20%. The velocity directions are defined in

ANSYS FLUENT with x-, y- and z-coordinates, where only the value at z-x-plane (horizontal plane) changes from case to case. The details are given in Table 4.8.

The results in Figure 4.25, Figure 4.26 and Figure 4.27 show that Test 17 gives the best comfort level.

Table 4.8.   Test design for the study of passenger-seat thermal comfort: horizontal velocity direction

Component	Location	Velocity magnitude	Velocity direction		
		m/s	17	18	19
Inlet 6 (left)	On the side wall (middle)	1.4	(1, 0, 0.3)	(1, 0, 0.7)	(1, 0, 1)
Inlet 6 (right)	On the side wall (middle)	1.4	(-1, 0, 0.3)	(-1, 0, 0.7)	(-1, 0, 1)
Inlet 7 (left)	On the side wall (top)	1.4	(1, -1, 0.3)	(1, -1, 0.7)	(1, -1, 1)
Inlet 7 (right)	On the side wall (top)	1.4	(-1, -1, 0.3)	(-1, -1, 0.7)	(-1, -1, 1)
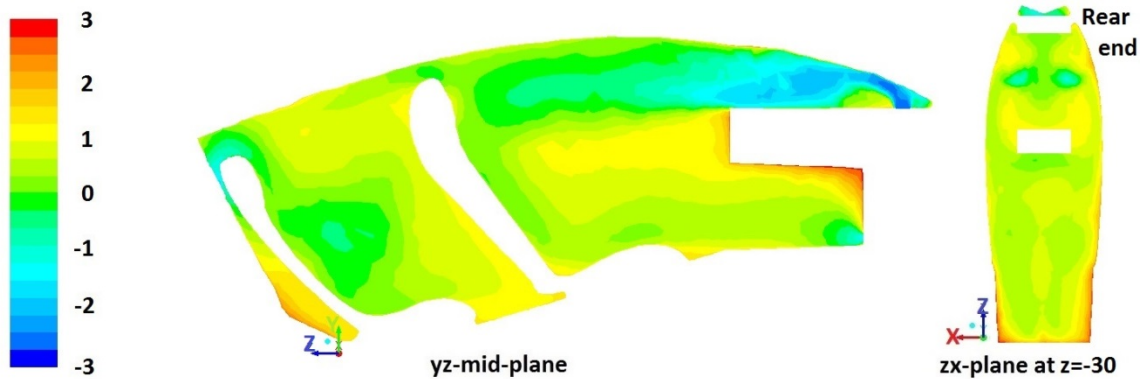
Figure 4.25.   PMV contour: Test 17
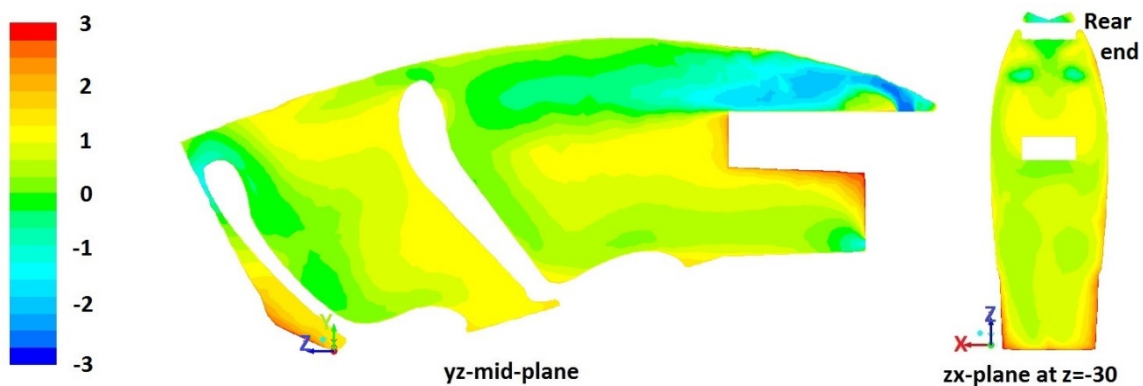
Figure 4.26.   PMV contour: Test 18
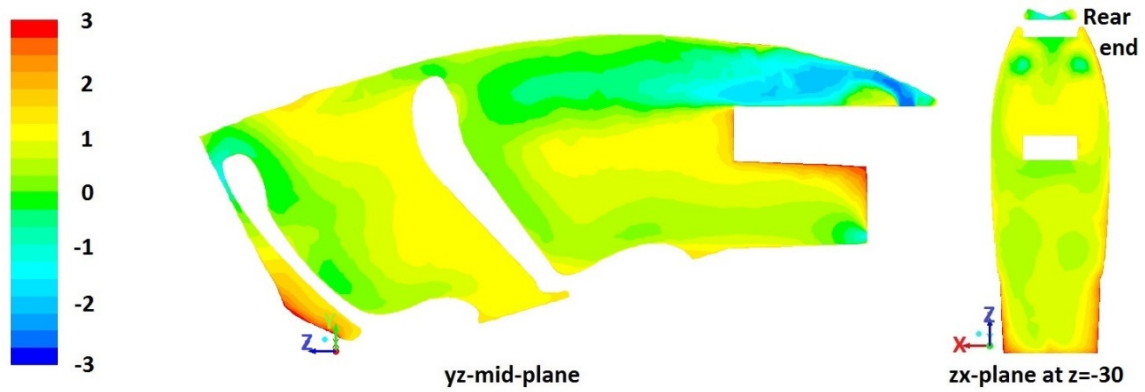
Figure 4.27.   PMV contour: Test 19

Effect of Vertical Velocity Direction

To investigate the effect of vertical velocity direction of Inlet 7, three scenarios are tested with the air flow rate is increased by 20%. The value at x-y-plane (vertical plane) changes from case to case. The details are given in Table 4.9.

The results in Figure 4.28, Figure 4.29 and Figure 4.30 show that Test 20 gives the best comfort level.

Table 4.9.   Test design for the study of passenger-seat thermal comfort: vertical velocity direction

Component	Location	Velocity magnitude	Velocity direction		
		m/s	20	21	22
Inlet 7 (left)	On the side wall (top)	1.4	(1, -0.5, 0.3)	(1, -2, 0.3)	(1, -5, 0.3)
Inlet 7 (right)	On the side wall (top)	1.4	(-1, -0.5, 0.3)	(-1, -2, 0.3)	(-1, -5, 0.3)
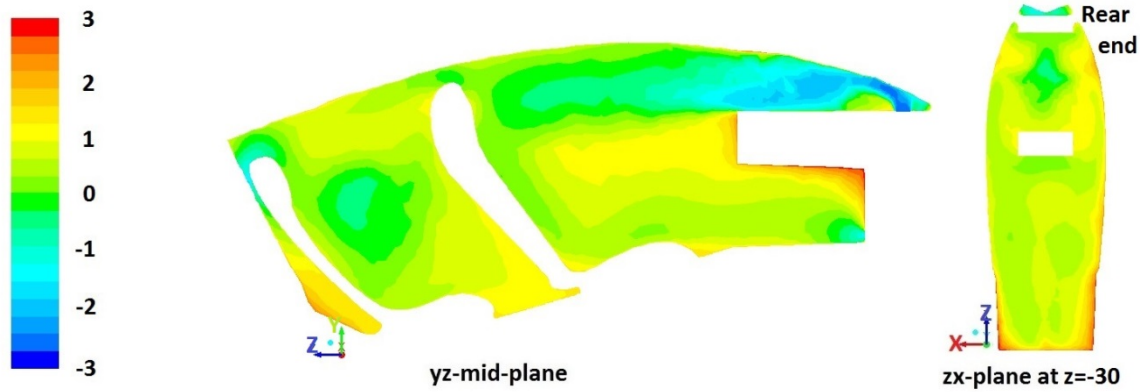
Figure 4.28. PMV contour: Test 20
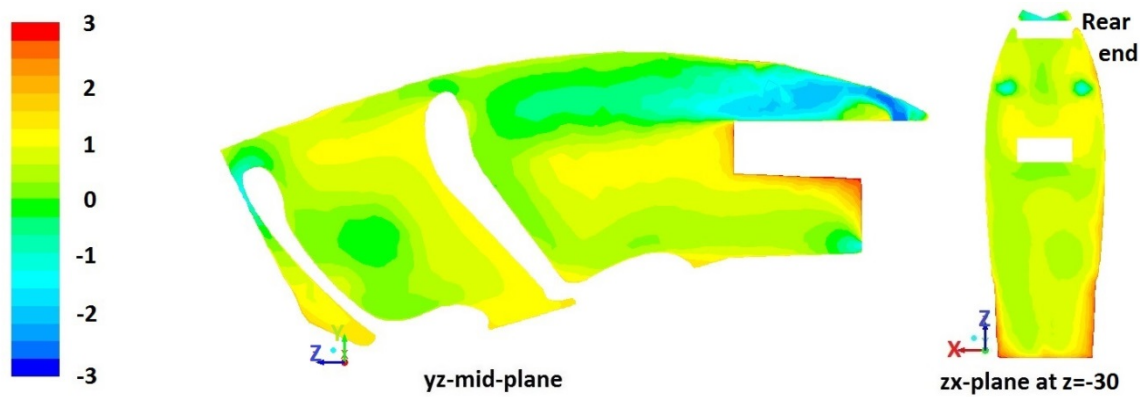
Figure 4.29. PMV contour: Test 21
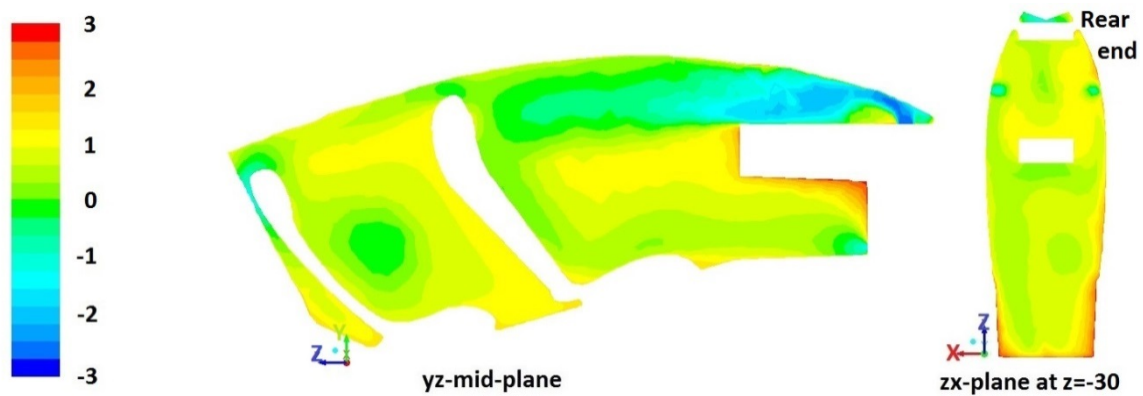
Figure 4.30. PMV contour: Test 22

4.2.3. Energy Consumption Analysis

The cooling power can be calculated from the Total Heat Transfer Rate command in ANSYS FLUENT by summing the total heat transfer rate through a boundary as Eq. (4.5) at inlet(s) [57]. The fan power consumption is calculated from

Bernoulli equation (Eq. 3.10) at inlet surface(s). The summary of all scenarios is shown in Table 4.10 and Figure 4.31.

$$q = q_c + q_r \qquad (4.5)$$

where q is cooling power, W/m^2 ; q_c is the convective heat transfer rate, W/m^2 ; q_r is the radiation heat transfer rate, W/m^2 . For flow boundaries, the total heat transfer rate is the flow rate of the conserved quantity.

It is easy to notice that the fan power is negligible compared to the cooling power consumption. But it is worth mentioning that the fan power is mostly related to the dimensions of outlet vent area. Fan power decreases when the outlet area increases. However, the outlet area has no influence on the cooling power consumption.

In general, the cooling power consumption is related to the air flow rate, and the variation of cooling load is negligible for fixed air flow rate values. However, the air flow pattern also shows a significant effect on the cooling load. For instance, when Test 17, Test 18, and Test 19 are compared to each other, it is noticeable that the cooling power consumption increases due to the better mixture of the hot and cold air. Test 20, Test 21, and Test 22 indicate the same trend as well. This phenomenon also explains the reason that when the air flow rate is increased by 20% in Tests 17, 18, 19, 21, 22, the cooling power does not increase or it even decreases.

It is observed that Test 20 achieves the best thermal comfort level among the various scenarios, but at the expense of higher energy consumption.

One may wonder why a parameter like volume-averaged-PMV is not used as the evaluation criteria. The reason can be clarified when Scenario 20 is compared to Scenario 13. The power consumptions for two scenarios vary little from each other. However, it can be tell from the PMV contours that Scenario 20 is more comfortable. As a conclusion, volume-averaged-PMV is not an accurate indication of thermal comfort.

Table 4.10.   Power consumption

Test #	Cooling power	Fan power	Total power
	w	w	w
1	671	8	679
2	671	1	672
3	671	4	675
4	671	4	681
5	668	4	672
6	667	4	671
7	672	4	676
8	761	6	767
9	761	2	763
10	963	4	967
11	969	4	973
12	963	4	967
13	967	4	971
14	964	4	968
15	959	4	963
16	963	4	967
17	965	4	969
18	917	4	921
19	879	3	882
20	981	4	985
21	936	4	940
22	902	4	906
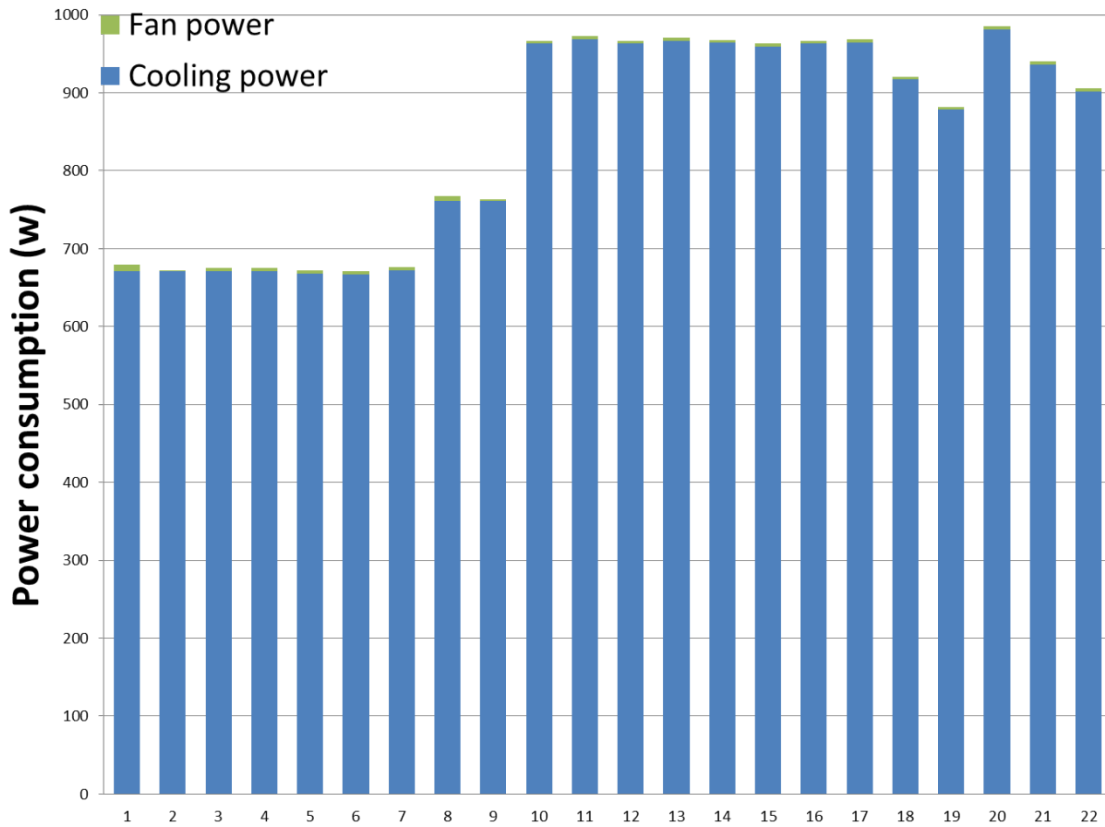
Figure 4.31. Power consumption

4.2.4. Transient Simulation: Pull-down Time

An important factor in the design of vehicle air conditioning systems is the pull-down time. Pull-down time is defined as the time required for the cabin temperature to fall from the hot soak condition down to the thermal comfort level. A transient simulation is performed to estimate the pull-down process of eVaro.

In the simulations of this study, only the thermal inertia of the cabin air contributes to the heat balance of the cabin air. We can assume the heat balance of the cabin to happen in the following general form:

$$\dot{Q} = mc\frac{dT}{dt} \tag{4.6}$$

where $\dot{Q}$ is the total cabin heat gains, m is the total cabin air mass, and c_p is the cabin air specific heat. For the simulated scenario, the solution to the above heat balance equation is of the form:

$$T = 20 + 25\exp(-\beta t) \tag{4.7}$$

where T is in °C. β is a constant directly proportional to the overall cabin heat transfer coefficient, and inversely proportional to the total cabin thermal inertia. It depends on the detailed geometry and simulation conditions and can be correlated by curve fitting the simulation results.

Since the air flow distribution is numerically solved in this work, the above analysis can be used to find a proper correlation for the transient thermal response of the cabin in the pull-down scenario. As shown in Figure 4.32, the following correlation is in excellent agreement with the transient results:

$$T = 20 + 25\exp(-0.11t) \tag{4.8}$$

According to the cabin air volume and specific heat, the cabin air has a thermal inertia of $700\,J/°C$. In case we add the thermal inertia of the cabin masses, which is $5600\,J/°C$ [14], the total cabin thermal inertia will be $6300\,J/°C$. Thus, for the case where the thermal masses are also considered, we will have $\beta = (0.11)(700/6300) = 0.012$. Therefore, the correlation for the transient response of the system will be:

$$T = 20 + 25\exp(-0.012t) \tag{4.9}$$

which yields to a pull-down time of 6 minutes as observed in Figure 4.32. Using the above analysis, we have included the effect of the thermal inertia of cabin masses without repeating the numerical simulations or making the numerical model complicated. The actual pull-down time is calculated based on the thermal response of the cabin air without including the complexity of the thermal masses in numerical simulations.
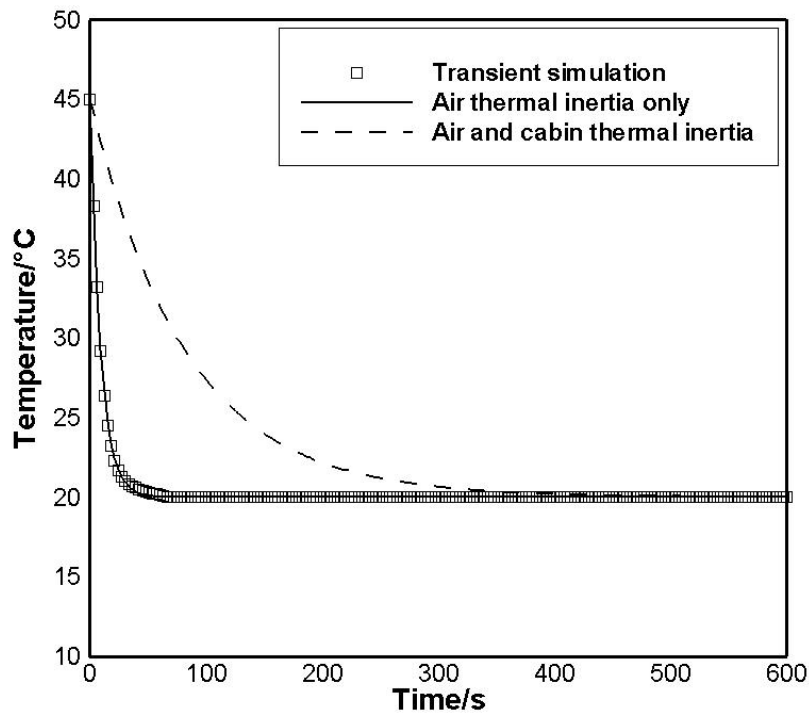
Figure 4.32.   Transient simulation results for calculating pull-down time

4.3.   Conclusions

A comprehensive and systematic numerical study is done for the eVaro vehicle cabin model.   In order to obtain a better mesh quality, a few modifications are implemented on the geometry at SolidWorks and ICEM CFD level.   As concluded from previous chapter, the mesh uses a boundary layer with y plus value in the range of viscous sublayer region; Realizable $k - \varepsilon$ Model and Non-Equilibrium Wall Function is applied to the simulation with the default parameters.

Due to the uniqueness of the present vehicle cabin model, the interaction between the thermal comfort levels of driver seat region and passenger seat region are negligible.   Therefore, the two regions are studied separately.   Cases are compared to each other when the air flow rate is constant.   It is concluded for the thermal comfort level of driver seat region:

- The front outlet at the foot region is important, while the effect of rear outlet is negligible.

- The middle inlet on the panel is unnecessary. It misleads the air flow from windshield inlets and disturbs the formation of air curtain at the top surface of vehicle cabin.

- A certain velocity magnitude is required for the windshield inlet to assure the formation of air curtain over the top surface. Taking the standard air velocity of thermal comfort into consideration, 2 m/s is proposed for this application.

It is concluded for the thermal comfort level of passenger seat region:

- An inlet behind the front seat, which is a conventional design for air flow system of sedan car cabin, is tested. However, there is no significant improvement of thermal comfort level.

- The rear outlet behind the rear seat is important.

- A uniformly distributed inlet design on the side wall gives a better performance over single vents.

- The velocity direction of side wall inlets plays an important role in the thermal comfort level, and optimized vectors are proposed for both in horizontal and vertical directions.

As such, a unique design of air flow system is obtained for the two-seat eVaro vehicle cabin model. The practicality is to be evaluated. Further optimization can be done with the cooperation of the manufacturing experts.

Chapter 5.

Conclusions and Future Work

5.1. Conclusions

Air flow distribution and thermal comfort in an HEV named eVaro was studied and simulations were performed to investigate the optimum air distribution pattern for providing thermal comfort while maintaining energy efficiency. A systematic approach was followed to use analytical, experimental, and numerical methods for finding the most efficient air distribution pattern.

In the first step, an analytical model of air flow inside a cavity was developed. Based on the engineering insight acquired by the analytical model results, experimental tests were designed. A testbed was built in Laboratory for Alternative Energy Conversion (LAEC), Simon Fraser University (SFU) to mimic the cabin of a vehicle. The main components of the testbed were a heater-fan installed inside a chamber enclosure which was vented through a ventilation unit. Temperatures at each wall, inlet air, and some points inside the chamber were recorded using a Data Acquisition (DAQ) system and temperature data loggers. In addition, the heater power and fan velocity were measured. Four scenarios with different heater-fan input were tested and the results were reported.

To develop a valid numerical model, the geometry of the experimental testbed was replicated into the ANSYS FLUENT software. The four experimental scenarios were simulated numerically and different grid distribution and turbulence models were examined. The numerical results were compared with the experimental data. It was concluded from the evaluation that:

- The boundary mesh type plays a significant role in the simulation accuracy, and $y^+ < 5$ shows the best performance.

- The Realizable $k - \varepsilon$ turbulence model produces the best simulation accuracy for the application of air flow distribution in vehicle cabins.

Therefore, the chosen numerical model was implemented for the analysis of eVaro cabin model. The cabin was divided into the driver seat and passenger seat regions, and asymmetrical ventilation was considered for the sake of energy efficiency. Seven steady-state scenarios were tested for studying the driver seat thermal comfort level, while fifteen simulations were performed for the passenger seat. The location of inlet and outlet, the air flow rate of inlets, and the direction of inlet air velocity were incorporated in the study scenarios. The simulation results were evaluated through their corresponding energy consumption and PMV values. In addition, a transient case study was performed to estimate the pull-down time to the steady-state temperature.

Some conventional vent arrangements were proved to be impractical for eVaro vehicle model, as a result of its tandem seat design. Personalized Ventilation (PV) was proposed in the present study. From the air flow distribution study of the eVaro model, it is concluded that:

- The driver and passenger seat regions are isolated from each other in terms of air distribution, and they have little influence on each other.

- The location of outlets affects the thermal comfort dramatically.

- The location of vents, the air flow velocity, and the inlet flow direction determine the air flow pattern inside the vehicle cabin.

- Compared to temperature, PMV is a more comprehensive and straight-forward index for estimation of the thermal comfort level.

- The air conditioning energy consumption and thermal comfort level have negligible correlation with the air flow rate.

- A trade-off exists between the thermal comfort level and HVAC energy consumption in the vehicle.

67

- An optimized air flow distribution needs to be designed to achieve improved thermal comfort level as well as energy efficiency.

5.2. Future Work

The focus of the present study was the optimization of air flow distribution inside eVaro vehicle model. The vent arrangements, energy consumption, and thermal comfort level were investigated for the worst case scenario. A further study may cover the following subjects:

- To analyze the thermal comfort level furthermore through adding a Physiological Manikin Model (PMM) to the present model.

- To investigate the interaction of the air flow distribution system with different environmental situations through coupling the CFD simulations with Energy Simulation (ES) modules that estimate the variation of thermal loads.

- To obtain a more comprehensive energy analysis through coupling the CFD simulations with a Vapour Compression Refrigeration (VCR) simulation module that estimates the energy consumption by the HVAC system. The effect of the inlet opening of the passenger region on the air flow rate of the driver region can be taken into consideration.

- Noise level study is recommended.

References

[1] L. D. Frank, M. a Andresen, and T. L. Schmid, "Obesity relationships with community design, physical activity, and time spent in cars.," *Am. J. Prev. Med.*, vol. 27, no. 2, pp. 87–96, Aug. 2004.

[2] Magazine article: "First Air-Conditioned Auto," *Popular Science*, p. 30, 1933.

[3] R. Farrington and J. Rugh, "Impact of vehicle air-conditioning on fuel economy, tailpipe emissions, and electric vehicle range," in *Earth Technologies Forum*, 2000.

[4] M. A. Lambert and B. J. Jones, "Automotive adsorption air conditioner powered by exhaust heat. part 1: conceptual and embodiment design," *Proc. Inst. Mech. Eng. Part D J. Automob. Eng.*, vol. 220, no. 7, pp. 959–972, 2006.

[5] R. Farrington, M. Cuddy, M. Keyser, and J. Rugh, "Opportunities to reduce air-conditioning loads through lower cabin soak temperatures," in *Proceedings of the 16th Electric Vehicle Symposium*, 1999.

[6] N. Djongyang, R. Tchinda, and D. Njomo, "Thermal comfort: A review paper," *Renew. Sustain. Energy Rev.*, vol. 14, no. 9, pp. 2626–2640, Dec. 2010.

[7] ASHRAE Standard, "thermal environmental conditions for human occupancy," *ASHRAE Stand. 55*.

[8] R. Yao, B. Li, and J. Liu, "A theoretical adaptive model of thermal comfort-Adaptive Predicted Mean Vote (aPMV)," *Build. Environ.*, vol. 44, no. 20, pp. 89–96, 2009.

[9] P. Taylor, R. J. Fuller, and M. B. Luther, "Energy use and thermal comfort in a rammed earth office building," *Energy Build.*, vol. 40, pp. 793–800, 2008.

[10] A. Wagner, E. Gossauer, C. Moosmann, T. Gropp, and R. Leonhart, "Thermal comfort and workplace occupant satisfaction-Results of field studies in German low energy office buildings," *Energy Build.*, vol. 39, no. 7, pp. 58–69, 2007.

[11] F. Bauman, A. Baughman, G. Carter, and E. A. Arens, "A field study of PEM (Personal Environmental Module) performance in Bank of America's San Francisco office buildings," 1997.

[12] M. Fountain, G. Brager, E. Arens, F. Bauman, and C. Benton, "Comfort control for short-term occupancy," *Energy Build.*, vol. 21, pp. 1–13, 1994.

[13]   M. Chludzinska and A. Bogdan, "Individual ventilation -- users' whim or economically justified energy saving," *Ciepłownictwo, Ogrzew. Went.*, vol. 2, pp. 32–34, 2008.

[14]   M. A. Fayazbakhsh and M. Bahrami, "Comprehensive Modeling of Vehicle Air Conditioning Loads Using Heat Balance Method," *SAE Int.*, Apr. 2013.

[15]   Y. Zheng, B. Mark, and H. Youmans, "A simple method to calculate vehicle heat load," *SAE Int.*, 2011.

[16]   O. Arici, S. Yang, D. Huang, and E. Oker, "Computer model for automobile climate control system simulation and application," *Int. J. Appl. Thermodyn.*, vol. 2, no. 2, pp. 59–68, 1999.

[17]   J. Selow, M. Wallis, S. Zoz, and M. Wiseman, "Towards a virtual vehicle for thermal analysis," *SAE Tech. Pap. 971841*, 1997.

[18]   H. Khayyam, A. Z. Kouzani, and E. J. Hu, "Reducing energy consumption of vehicle air conditioning system by an energy management system," *2009 IEEE Intell. Veh. Symp.*, vol. i, no. 1, pp. 752–757, Jun. 2009.

[19]   K. C. Wei and G. A. Dage, "An intelligent automotive climate control system," *IEEE Int. Conf. Syst. Man Cybern. Intell. Syst. 21st Century*, 1995.

[20]   V. M. Thomas, A. K. Meier, S. G. Gunda, and T. P. Wenzel, "Cars are buildings: Building-like energy use in automobiles," *Transp. Res. Part D Transp. Environ.*, vol. 16, no. 4, pp. 341–345, Jun. 2011.

[21]   US Environmental Protection Agency, "Proposed rulemaking to establish light-duty vehicle greenhouse gas emission standards and corporate average fuel economy standards," vol. 74, pp. 49454–49789, 2009.

[22]   R. G. Bosch, *Automotive Handbook*, Fourth Edi. Cambridge, US: Bentley Publishers, 1996.

[23]   Website: F. V. Technologies, "http://www.futurevehicletechnologies.com." .

[24]   M. B. Glauert, "The Wall Jet," *J. Fluid Mech.*, vol. 1, no. 06, pp. 625–643, 1956.

[25]   Z. Zhai, Q. Chen, P. Haves, and J. H. Klems, "On approaches to couple energy simulation and computational fluid dynamics programs," *Build. Environ.*, vol. 37, pp. 857–864, 2002.

[26]   W. Yan, Y. Zhang, Y. Sun, and D. Li, "Experimental and CFD study of unsteady airborne pollutant transport within an aircraft cabin mock-up," *Build. Environ.*, vol. 44, no. 1, pp. 34–43, Jan. 2009.

[27]   T. Zhang and Q. (Yan) Chen, "Novel air distribution systems for commercial aircraft cabins," *Build. Environ.*, vol. 42, no. 4, pp. 1675–1684, Apr. 2007.

[28]   V. Bianco, O. Manca, S. Nardini, and M. Roma, "Numerical investigation of transient thermal and fluidynamic fields in an executive aircraft cabin," *Appl. Therm. Eng.*, vol. 29, no. 16, pp. 3418–3425, Nov. 2009.

[29]   G. Günther, J. Bosbach, J. Pennecot, C. Wagner, T. Lerche, and I. Gores, "Experimental and numerical simulations of idealized aircraft cabin flows," *Aerosp. Sci. Technol.*, vol. 10, no. 7, pp. 563–573, Oct. 2006.

[30]   J. Bosbach, J. Pennecot, C. Wagner, M. Raffel, T. Lerche, and S. Repp, "Experimental and numerical simulations of turbulent ventilation in aircraft cabins," *Energy*, vol. 31, no. 5, pp. 694–705, Apr. 2006.

[31]   Z. Zhang, X. Chen, S. Mazumdar, T. Zhang, and Q. Chen, "Experimental and numerical investigation of airflow and contaminant transport in an airliner cabin mockup," *Build. Environ.*, vol. 44, no. 1, pp. 85–94, Jan. 2009.

[32]   M. Tapsoba, J. Moureh, and D. Flick, "Airflow patterns inside slotted obstacles in a ventilated enclosure," *Comput. Fluids*, vol. 36, no. 5, pp. 935–948, Jun. 2007.

[33]   J. Moureh, N. Menia, and D. Flick, "Numerical and experimental study of airflow in a typical refrigerated truck configuration loaded with pallets," *Comput. Electron. Agric.*, vol. 34, no. 1–3, pp. 25–42, May 2002.

[34]   J. Moureh and D. Flick, "Wall air–jet characteristics and airflow patterns within a slot ventilated enclosure," *Int. J. Therm. Sci.*, vol. 42, no. 7, pp. 703–711, Jul. 2003.

[35]   O. Yongson, I. A. Badruddin, Z. a. Zainal, and P. a. Aswatha Narayana, "Airflow analysis in an air conditioning room," *Build. Environ.*, vol. 42, no. 3, pp. 1531–1537, Mar. 2007.

[36]   G. Tong, G. Zhang, D. M. Christopher, B. Bjerg, Z. Ye, and J. Cheng, "Evaluation of turbulence models to predict airflow and ammonia concentrations in a scale model swine building enclosure," *Comput. Fluids*, Nov. 2012.

[37]   J. Posner, C. Buchanan, and D. Dunn-Rankin, "Measurement and prediction of indoor air flow in a model room," *Energy Build.*, vol. 35, no. January 2002, 2003.

[38]   S. M. Salim and S. C. Cheah, "Wall y+ strategy for dealing with wall-bounded turbulent flows," *Proc. Int. MultiConference Eng. Comput. Sci.*, vol. II, 2009.

[39]   M. Ariff, S. M. Salim, and S. C. Cheah, "Wall y+ approach for dealing with turbulent flow over a surface mounted cube: part 2 - high reynolds number," *Seventh Int. Conf. CFD Miner. Process Ind.*, no. December, pp. 1–6, 2009.

[40]   C. Wu and N. a. Ahmed, "A novel mode of air supply for aircraft cabin ventilation," *Build. Environ.*, vol. 56, pp. 47–56, Oct. 2012.

[41]   W. Liu, S. Mazumdar, Z. Zhang, S. B. Poussou, J. Liu, C.-H. Lin, and Q. Chen, "State-of-the-art methods for studying air distributions in commercial airliner cabins," *Build. Environ.*, vol. 47, pp. 5–12, Jan. 2012.

[42]   H. Zhang, L. Dai, G. Xu, Y. Li, W. Chen, and W.-Q. Tao, "Studies of air-flow and temperature fields inside a passenger compartment for improving thermal comfort and saving energy. Part I: Test/numerical model and validation," *Appl. Therm. Eng.*, vol. 29, no. 10, pp. 2022–2027, Jul. 2009.

[43]   H. Zhang, L. Dai, G. Xu, Y. Li, W. Chen, and W. Tao, "Studies of air-flow and temperature fields inside a passenger compartment for improving thermal comfort and saving energy. Part II: Simulation results and discussion," *Appl. Therm. Eng.*, vol. 29, no. 10, pp. 2028–2036, Jul. 2009.

[44]   T. Han, L. Huang, S. Kelly, C. Huizenga, and H. Zhang, "Virtual thermal comfort engineering," *SAE Int.*, 2001.

[45]   A. Alexandrov, "Analysis of flow patterns and heat transfer in generic passenger car mini-environment," *9th Annu. Conf. CFD Soc. Canada*, pp. 27–29, 2001.

[46]   I. Bayraktar, "Time dependent simulation methods for vehicle thermal management," *Proc. 2009 Gr. Veh. Syst. Eng. Technol. Symp.*, pp. 1–4, 2009.

[47]   I. Bayraktar, "Computational simulation methods for vehicle thermal management," *Appl. Therm. Eng.*, vol. 36, pp. 325–329, Apr. 2012.

[48]   a. Alahmer, A. Mayyas, A. a. Mayyas, M. a. Omar, and D. Shan, "Vehicular thermal comfort models; a comprehensive review," *Appl. Therm. Eng.*, vol. 31, no. 6–7, pp. 995–1002, May 2011.

[49]   Y. Cheng, J. Niu, and N. Gao, "Thermal comfort models: A review and numerical investigation," *Build. Environ.*, vol. 47, pp. 13–22, Jan. 2012.

[50]   Q. Chen, "Ventilation performance prediction for buildings: A method overview and recent applications," *Build. Environ.*, vol. 44, no. 4, pp. 848–858, Apr. 2009.

[51]   Q. Chen, K. Lee, S. Mazumdar, S. Poussou, L. Wang, M. Wang, and Z. Zhang, "Ventilation performance prediction for buildings: model assessment," *Build. Environ.*, vol. 45, no. 2, pp. 295–303, Feb. 2010.

[52]   M. Cisternino, "Thermal climate in cabs and measurement problems," *CABCLI Semin.*, 1999.

[53]   Working paper: J. Malchaire, "Ergonomics of the thermal environment - determination of metabolic heat production," 2001.

[54]   Report: K. Parsons, Loughborough University, UK, "The estimation of metabolic heat for use in the assessment of thermal comfort," 1989.

[55]   L. Huang and T. Han, "Validation of 3-D passenger compartment hot soak and cool-down analysis for virtual thermal comfort engineering reprinted from : progress in climate control technologies," *SAE Int.*, 2002.

[56]   B. E. Launder and D. B. Spalding, *Lectures in Mathematical Models of Turbulence.* London, England: Academic Press, 1972.

[57]   ANSYS FLUENT help document, 2011.

Appendix A.

User Defined Function (UDF) for PMV Calculation

```
#include "udf.h"
DEFINE_ON_DEMAND(Comfort)
{
 Domain *d;
 Thread *t;
 cell_t c;

 real CLO;                                        // Clothing (clo)
 real MET;                                        // Metabolic rate (met)
 real WME;                             // External work, normally around 0 (met)
 real TA;                                         // Air temperature (°C)
 real TR;                                    // Mean radiant temperature (°C)
 real VEL;                                     // Relative air velocity (m/s)
 real RH;                                         // Relative humidity (%)
 real PA;                                       // Water vapour pressure (Pa)

 real FNPS;                                  // Saturated vapour pressure, kPa
 real ICL;                                    // Clothing insulation, m2K/W
 real TCL;                                 // Clothing surface temperature, °C
 real M;                                       // Metabolic rate, W/m2
 real W;                                       // External work, W/m2
 real MW;                        // Internal heat production in the human body, W/m2
 real FCL;                                        // Clothing area factor
 real HCF;                      // Forced convective heat transfer coefficient, W/m2K
 real HCN;                     // Natural convective heat transfer coefficient, W/m2K
 real HC;                          // Convective heat transfer coefficient, W/m2K
 real TAA;                                        // Air temperature, K
 real TRA;                                 // Mean radiant temperature, K
 real HL1;                                   // Heat loss difference through skin
 real HL2;                                    // Heat loss by sweating (comfort)
```

```
real HL3;                                           // Latent respiration heat loss
real HL4;                                           // Dry respiration heat loss
real HL5;                                           // Heat loss by radiation
real HL6;                                           // Heat loss by convection
real TS;                                            // Thermal sensation transfer coefficient

real EPS;                                           // Small value
real i;                                             // Iterator
real TCLA;                                          // First guess for surface temperature of clothing
real P1,P2,P3,P4,P5;                                // Calculation terms
real XN,XF;                                         // Iterative solutions
real PMV,PPD;                                       // Predicted mean vote and predicted percentage dissatisfied

d=Get_Domain(1);

EPS=0.00015;
CLO=1.0;
MET=1.0;
WME=0.0;
RH=50.0;

ICL=0.155*CLO;
M=MET*58.15;
W=WME*58.15;
MW=M-W;
if (ICL<=0.078) FCL=1.0+1.29*ICL; else FCL=1.05+0.645*ICL;

thread_loop_c(t,d)
{
begin_c_loop(c,t)
{
TA=C_T(c,t)-273;
TR=35;
VEL=sqrt(pow(C_U(c,t),2)+pow(C_V(c,t),2)+pow(C_W(c,t),2));
```

```
FNPS=exp(16.6536-4030.183/(TA+235));
PA=RH*10.0*FNPS;
HCF=12.1*sqrt(VEL);
TAA=TA+273.0;
TRA=TR+273.0;

TCLA=TAA+(35.5-TA)/(3.5*(6.45*ICL+0.1));
P1=ICL*FCL;
P2=P1*3.96;
P3=P1*100;
P4=P1*TAA;
P5=308.7-0.028*MW+P2*pow(TRA/100,4);
XN=TCLA/100.0;
XF=XN;

for (i=0;i<150;i++)
{
XF=(XF+XN)/2.0;
HCN=2.38*pow(fabs(100.0*XF-TAA),0.25);
if (HCF>HCN) HC=HCF; else HC=HCN;
XN=(P5+P4*HC-P2*pow(XF,4))/(100+P3*HC);
if (fabs(XN-XF)<EPS) break;
}

TCL=100.0*XN-273.0;
HL1=3.05*0.001*(5733.0-6.99*MW-PA);
if (MW>58.15) HL2=0.42*(MW-58.15); else HL2 = 0;
HL3=1.7*0.00001*M*(5867.0-PA);
HL4=0.0014*M*(34.0-TA);
HL5=3.96*FCL*(pow(XN,4)-pow(TRA/100.0,4));
HL6=FCL*HC*(TCL-TA);

TS=0.303*exp(-0.036*M)+0.028;
```

```
PMV=TS*(MW-HL1-HL2-HL3-HL4-HL5-HL6);
PPD=100.0-95.0*exp(-0.03353*pow(PMV,4)-0.2179*pow(PMV,2));

C_UDMI(c,t,0)=PMV;
C_UDMI(c,t,1)=PPD;
}
end_c_loop(c,t)
}
}
```

Appendix B

Semi-Analytical Study of Cavity Air Flow

Automotive Heating, Ventilation and Air-Conditioning (HVAC) systems are designed to provide thermal comfort for vehicle passengers. A desirable driving condition, as well as a more efficacious system, rather than a system simply with high heating/cooling capacity is definitely preferable. Consequently, the study of air flow pattern in cabin is a key element for the upgrade of automotive HVAC systems. However, practical compact relationships for implementation in real-time control systems resulting from experimental and/or numerical data are scarce.

Numerous previous studies have been devoted to numerical simulations, using approaches such as CFD[1], [2] and the zonal model[3], [4]. However, a major problem associated with numerical simulation is the computational time consumption. Several hours to several days of calculation time is normally necessary to acquire the solution to a single simulation case. Additionally, it is not feasible to include numerical simulations in a vehicle computer module to simulate every new condition encountered on the go in real-time. As such, development of compact models that can predict the cabin conditions is highly beneficial for automotive HVAC engineers.

For this purpose, we have to seek the solution back into the essential studies. Analytical and experimental studies over simple flow patterns like jet flow [5], [6] have started since early last century. They laid a solid foundation for the modern applications and can be used as building-blocks, which the engineers and researchers still benefit from.

This semi-analytical model is to record the flow pattern in a cavity or cavity-similar geometry. By dividing the cavity into certain subdomains, each subdomain can be represented by either free jet or plane wall jet. Then, the local coordinates are converted into the global coordinates and the subdomains are superimposed into the whole flow pattern. It is validated that when the inlet velocity changes, the flow pattern doesn't change, but the velocity magnitude changes proportionally. A cavity, with an inlet and an outlet at each end of a side wall, is taken as an example to explain the

methodology. The cavity is divided into four subdomains and each of them is represented by a plane wall jet flow. The result is compared against the numerical simulation. For an abiding geometry, the current model is able to predict the flow pattern.

Unit Velocity Profiles

It is concluded from the author's observation that regardless of the complexity of the geometry, the air flow marches forward either freely or attached to a wall. Therefore, the classic solutions for free jet and plane wall jet are selected as the building blocks for present model. When $f(\eta) = u/U_{max}$ and $\eta = y/h_{hmv}$, the velocity profiles of plane free jet[7] and plane wall jet[6] can be denoted as:

$$f(\eta) = \exp\left(-0.693\eta^2\right) \tag{B.1}$$

and

$$f(\eta) = 1.4794\eta^{\frac{1}{7}}\left[1 - erf\left(0.67753\eta\right)\right] \tag{B.2}$$

where U_{max} is the maximum velocity at a certain cross-section; η is similarity parameter; h_{hmv} is height of the half maximum velocity.

In the followed methodology demonstration, there is no free jet involved. Therefore, only the plane wall jet expression is implemented.

Problem statement

A dimensionless square cavity with a side length of L is assumed. There is an air inlet at the bottom and an air outlet at the top of one side wall, with width s. The cavity is split into 4 parts, which are numbered according to the passing order of air flow. Only parallel velocity (local x-velocity) attached to the walls are taken into consideration since the building block is plane wall jet. u_1, u_2, u_3, and u_4 indicate the local x-velocity for each wall, as shown in Figure B.5.1.
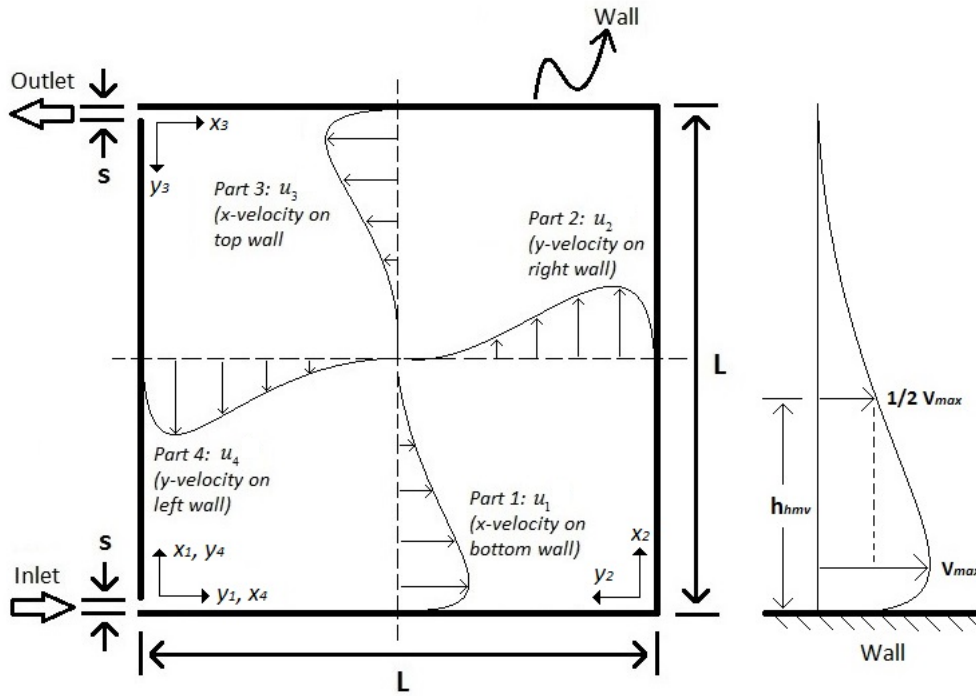
Figure B.5.1. Problem schematic: 2D cavity

In order to correlate and combine the solutions from the subdomains, we assume the following correlations:

$$u_{\max,n} = p_{1,n}x_n^3 + p_{2,n}x_n^2 + p_{3,n}x_n + p_{4,n} \tag{B.3}$$

$$h_{hmv,n} = q_{1,n}x_n^4 + q_{2,n}x_n^3 + q_{3,n}x_n^2 + q_{4,n}x_n + q_{5,n} \tag{B.4}$$

where the p's and q's are correlation constants, n is the corresponding subdomain number. Using Eqs. (B.1) and (B.2), the dimensional velocity profile of a specific part is written as:

$$u_n = Uu_{\max,n}f_n(\eta_n) \tag{B.5}$$

The values at each location of the whole velocity field can be indicated as:

$$\vec{V} = \left(u_1\left(\frac{x_1}{L}, \frac{y_1}{L}\right) - u_3\left(\frac{x_2}{L}, \frac{L-y_2}{L}\right)\right)\vec{i} + \left(u_2\left(\frac{y_3}{L}, \frac{L-x_3}{L}\right) - u_4\left(\frac{y_4}{L}, \frac{x_4}{L}\right)\right)\vec{j} \tag{B.6}$$

where u_1, u_3, u_2, and u_4 are turned into global coordinates.

Validation of Flow Pattern

To test the similarity among the flow patterns with different inlet velocities, a few numerical simulations are done, where $L = 1$ m and $s = 0.05$ m . The magnitudes of velocity are 1 m/s, 2 m/s and 5 m/s, respectively. The dimensionless velocities (divided by the inlet velocity magnitude) at four cross-sections, $x = 0.2$, 0.4, 0.6 and 0.8 m , are compared to each other with the inlet velocity magnitude in Figure B.5.2. The velocities are scaled down by 5 times, in order to indicate a better demonstration. The velocity profiles collapse over each other very well, except the near wall regions show slightly differences. It should be noted that the thermal comfort requires an air flow velocity no more than 1 m/s. As such, the deviation is acceptable for vehicle HVAC application.

(a)   (b)
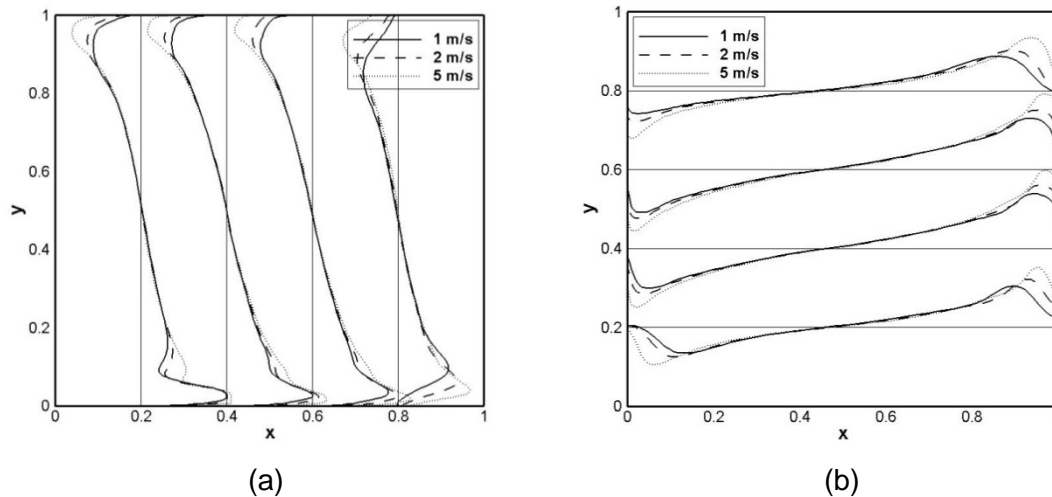
Figure B.5.2. Comparison of velocity at cross-sections: (a) x velocity; (b) y velocity

Obtaining u$_{max}$ and h$_{hmv}$

According to Eq. (B.5), the velocity profile is a function of the maximum velocity and the half maximum velocity height. To obtain these two parameters, numerical simulations with different variations of the inlet velocity value and slit widths are performed for an analysis of the functionality of the profile with respect to the inlet

velocity and slit width. After grid independence study, a cavity of $L^2 = 1\,\text{m} \times 1\,\text{m}$ with 22500 grids is chosen for ANSYS FLUENT simulation. Standard $k - \varepsilon$ turbulence model with wall enhanced treatment is set.

Both uniform and parabolic inlet velocity profiles have been considered in the preliminary stage of the study. The results show negligible difference, which means that the bulk of the flow is almost independent of the inlet velocity profile. Thus, uniform inlet velocity is used for the present study for simplicity.

To demonstrate the methodology, the case with $0.05\,\text{m}$ slit width is taken for example. u_{max} and h_{hmv} values on local cross-sections of $x = 0.1, 0.2...0.9\,\text{m}$ are picked up manually from numerical simulation results. The correlations as Eq. (B.3) and (B.4) are obtained through curve fitting for different slit widths, as shown in Table B.1.

Table B.1.   Curve fitting result: 0.05 m slit width

Part #	Formula
1	$u_{\text{max}} = -2.02x_3^3 + 0.630x_3^2 + 0.564x_3 + 0.935$ $h_{hmv} = 3.75x_3^4 - 6.68x_3^3 + 3.73x_3^2 - 0.539x_3 + 0.0740$
2	$u_{\text{max}} = 0.846x_3^3 - 4.31x_3^2 + 3.45x_3 + 0.141$ $h_{hmv} = 1.79x_3^4 - 3.86x_3^3 + 3.13x_3^2 - 1.01x_3 + 0.283$
3	$u_{\text{max}} = -0.495x_3^3 - 1.37x_3^2 + 1.49x_3 + 0.478$ $h_{hmv} = -1.12x_3^4 + 3.31x_3^3 - 3.11x_3^2 + 1.18x_3 + 0.0652$
4	$u_{\text{max}} = -2.13x_3^3 - 0.0364x_3^2 + 2.24x_3 - 0.0364$ $h_{hmv} = 7.49x_3^4 - 13.0x_3^3 + 7.69x_3^2 - 1.90x_3 + 0.389$

Having the velocity profiles of the four subdomains, we are enabled to combine them in the vector form to acquire the solution to the whole cavity problem. The velocity profiles from the analytical formulation are compared with the numerical results obtained from the ANSYS simulation software, as shown in Figure B.5.3.
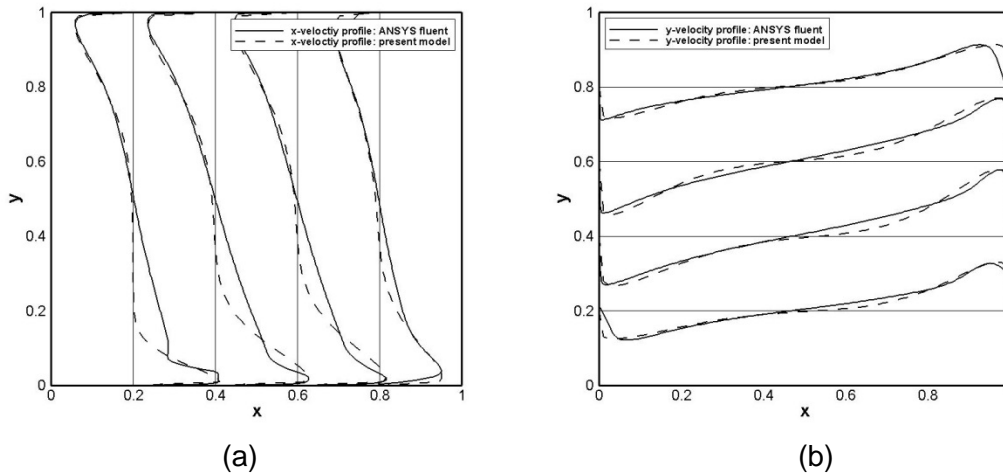
Figure B.5.3. **Comparison between the present model and numerical simulations with** 0.05 m **slit width: (a)** $x-$**velocity at vertical cross-sections; (b)** $y-$**velocity at horizontal cross-sections**

The semi-analytical results are in a good agreement with the numerical results. Some discrepancy is noticeable in subdomain part 1. The plane wall jet is assumed to develop from a jet originated from a point. But a uniform inlet velocity is assumed in the numerical simulation for the inlet. This is the major cause for the discrepancy between the velocity profile obtained from analytical model and numerical simulation. Changing the inlet velocity of the numerical simulations to profiles similar to the plane wall jet may help improve the validation. In contrast, when the airflow develops further from the inlet slit, better agreement between the analytical and numerical results is obtained.

The analytical results also differ at the corners. This issue can be neglected for practical applications, since the details of the flow and circulations may not be important for airflow inside a vehicle cabin.

In specific practical case, the geometry of cabin and slit width of registers are fixed for a certain car. Since the velocity field is not a function of inlet velocity magnitude, only one numerical simulation has to be done in advance for this specific case in order to get the data of maximum velocity and half maximum velocity height. Thus, the velocity field with different velocity can be calculated through the present model.
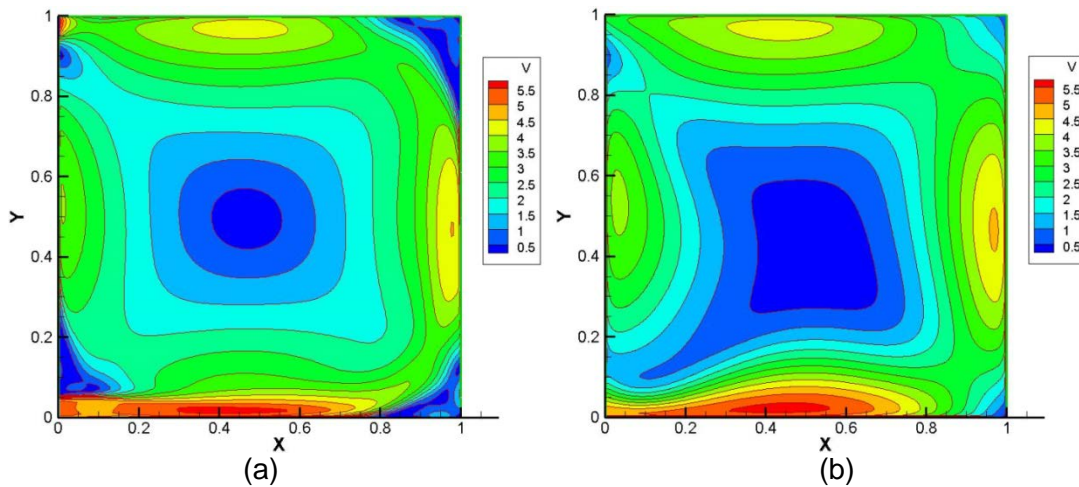
83

Figure B.5.4. Velocity magnitude contour of the cavity problem: (a) numerical simulation; (b) the present model

Figure B.5.4 compares the velocity magnitudes achieved from the semi-analytical and numerical simulations.   As well as the quantitative validation, it is qualitatively observed that the contour shapes also match.   It is hence proposed to use the semi-analytical compact relationship developed in this work instead of performing complex and time-consuming numerical simulations for further flow conditions.

Conclusions

A new semi-analytical method of solving the air flow pattern is demonstrated through a square cavity by using the similarity solution, numerical simulations, and the concept of superposition. An explicit compact expression for the vector field in the cavity is obtained.   The results show that the present model can provide engineers with an approximate velocity distribution in simple geometries, which is potential for real-time control of thermal comfort level in vehicle cabins. Addition of free wall jet calculations to the present model is recommended for future work.

References

[1]   A. Alexandrov, "Analysis of flow patterns and heat transfer in generic passenger car mini-environment," *9th Annu. Conf. CFD Soc. Canada*, pp. 27–29, 2001.

[2]   H. B. Nahor, M. L. Hoang, P. Verboven, M. Baelmans, and B. M. Nicolaï, "CFD model of the airflow, heat and mass transfer in cool stores," *Int. J. Refrig.*, vol. 28, no. 3, pp. 368–380, May 2005.

[3] M. O. Abadie, M. M. De Camargo, K. C. Mendonça, and P. Blondeau, "Improving the prediction of zonal modeling for forced convection airflows in rooms," *Build. Environ.*, vol. 48, pp. 173–182, 2012.

[4] H. Okuyama, Y. Onishi, S. Tanabe, and S. Kashihara, "Statistical data analysis method for multi-zonal airflow measurement using multiple kinds of perfluorocarbon tracer gas," *Build. Environ.*, vol. 44, no. 3, pp. 546–557, Mar. 2009.

[5] M. B. Glauert, "The Wall Jet," *J. Fluid Mech.*, vol. 1, no. 06, pp. 625–643, 1956.

[6] A. Verhoff, "The two-dimensional, turbulent wall jet with and without an external free stream," 1963.

[7] N. Rajaratnam, *Turbulent Jets*. Elsevier Ltd, 1976, p. 21.